



The Massive Ancient Galaxies at $z > 3$ NEar-infrared (MAGAZ3NE) Survey: Confirmation of Extremely Rapid Star Formation and Quenching Timescales for Massive Galaxies in the Early Universe*

Ben Forrest¹, Z. Cemile Marsan², Marianna Annunziatella^{3,4}, Gillian Wilson¹, Adam Muzzin², Danilo Marchesini³, M. C. Cooper⁵, Jeffrey C. C. Chan¹, Ian McConachie¹, Percy Gomez⁶, Erin Kado-Fong⁷, Francesco La Barbera⁸, Daniel Lange-Vagle³, Julie Nantais⁹, Mario Nonino¹⁰, Paolo Saracco¹¹, Mauro Stefanon¹², and Remco F. J. van der Burg¹³

¹ Department of Physics and Astronomy, University of California, Riverside, 900 University Avenue, Riverside, CA 92521, USA

² Department of Physics and Astronomy, York University, 4700, Keele Street, Toronto, ON M3J 1P3, Canada

³ Department of Physics and Astronomy, Tufts University, 574 Boston Avenue Suites 304, Medford, MA 02155, USA

⁴ Centro de Astrobiología (CSIC-INTA), Ctra de Torrejón a Ajalvir, km 4, E-28850 Torrejón de Ardoz, Madrid, Spain

⁵ Center for Cosmology, Department of Physics and Astronomy, University of California, Irvine, 4129 Frederick Reines Hall, Irvine, CA, USA

⁶ W. M. Keck Observatory, 65-1120 Mamalahoa Hwy., Kamuela, HI 96743, USA

⁷ Department of Astrophysical Sciences, 4 Ivy Lane, Princeton University, Princeton, NJ 08544, USA

⁸ INAF—Osservatorio Astronomico di Capodimonte, sal. Moiariello 16, I-80131 Napoli, Italy

⁹ Departamento de Ciencias Físicas, Universidad Andres Bello, Fernandez Concha 700, Las Condes 7591538, Santiago, Región Metropolitana, Chile

¹⁰ INAF—Osservatorio Astronomico di Trieste, Via G.B. Tiepolo 11, I-34143 Trieste, Italy

¹¹ INAF—Osservatorio Astronomico di Brera, via Brera 28, I-20121 Milano, Italy

¹² Leiden Observatory, Leiden University, 2300 RA Leiden, The Netherlands

¹³ European Southern Observatory, Karl-Schwarzschild-Str. 2, D-85748, Garching, Germany; benjamif@ucr.edu

Received 2020 August 4; revised 2020 September 9; accepted 2020 September 10; published 2020 October 30

Abstract

We present near-infrared spectroscopic confirmations of a sample of 16 photometrically selected galaxies with stellar masses $\log(M_*/M_\odot) > 11$ at redshift $z > 3$ from the XMM-VIDEO and COSMOS-UltraVISTA fields using Keck/MOSFIRE as part of the Massive Ancient Galaxies At $z > 3$ NEar-infrared (MAGAZ3NE) survey. Eight of the ultramassive galaxies (UMGs) have specific star formation rates (sSFR) $< 0.03 \text{ Gyr}^{-1}$, with negligible emission lines. Another seven UMGs show emission lines consistent with active galactic nuclei and/or star formation, while only one UMG has $\text{sSFR} > 1 \text{ Gyr}^{-1}$. Model star formation histories of these galaxies describe systems that formed the majority of their stars in vigorous bursts of several hundred megayear duration around $4 < z < 6$ during which hundreds to thousands of solar masses were formed per year. These formation ages of $< 1 \text{ Gyr}$ prior to observation are consistent with ages derived from measurements of $D_n(4000)$ and $EW_0(H\delta)$. Rapid quenching followed these bursty star-forming periods, generally occurring less than 350 Myr before observation, resulting in post-starburst SEDs and spectra for half the sample. The rapid formation timescales are consistent with the extreme star formation rates observed in $4 < z < 7$ dusty starbursts observed with ALMA, suggesting that such dusty galaxies are progenitors of these UMGs. While such formation histories have been suggested in previous studies, the large sample introduced here presents the most compelling evidence yet that vigorous star formation followed by rapid quenching is almost certainly the norm for high-mass galaxies in the early universe. The UMGs presented here were selected to be brighter than $K_s = 21.7$, raising the intriguing possibility that even (fainter) older quiescent UMGs could exist at this epoch.

Unified Astronomy Thesaurus concepts: Galaxy evolution (594); High-redshift galaxies (734); Quenched galaxies (2016)

1. Introduction

The observation of massive, quiescent galaxies has repeatedly forced astronomers to reconsider the paradigm of galaxy evolution and cosmology, particularly in the early universe. The spectrum of an old galaxy at $z = 1.55$ (Dunlop et al. 1996) brought serious challenges to the Einstein–de Sitter cosmology (Einstein & de Sitter 1932) popular at the time. Further observations of similar galaxies at progressively higher redshifts (e.g., Cimatti et al. 2004; Kriek et al. 2009; Gobat et al. 2012; van de Sande et al. 2013) led to the realization that

galaxies could build up large stellar populations and quench star formation at early times, which required new suites of simulations to reproduce them (e.g., Genel et al. 2014; Hopkins et al. 2014; Vogelsberger et al. 2014a, 2014b; Crain et al. 2015; Henriques et al. 2015; Schaye et al. 2015; Wellons et al. 2015; Davé et al. 2016; Feldmann et al. 2016).

It is now clear that most, if not all, ultramassive galaxies (UMGs; $\log(M_*/M_\odot) > 11$) have assembled the majority of their mass by $z \sim 1.5$ (e.g., Gallazzi et al. 2005; Nelan et al. 2005; Thomas et al. 2005; Treu et al. 2005; Thomas et al. 2010; Estrada-Carpenter et al. 2020). Indeed, the number density of these galaxies evolves very little over the most recent 9 Gyr (van der Wel et al. 2014; Gargiulo et al. 2016; Kawinwanichakij et al. 2020), and evidence suggests most of the mass assembly for these galaxies occurred in an early short-lived burst, while less massive quiescent galaxies underwent longer,

* The spectra presented herein were obtained at the W. M. Keck Observatory, which is operated as a scientific partnership among the California Institute of Technology, the University of California, and the National Aeronautics and Space Administration. The Observatory was made possible by the generous financial support of the W. M. Keck Foundation.

less intense periods of star formation (Pacifci et al. 2016; Ciesla et al. 2017). Thus, determining the evolution of these UMGs at earlier times is of great interest as they hold clues to the processes required not only for intense, early star formation, but also rapid quenching.

Critical to the discovery of large numbers of quiescent UMGs at higher redshifts is the existence of wide and deep near-infrared (NIR) imaging combined with ancillary multiwavelength observations. The NIR wavelengths are where these galaxies are most easily detected and also constrain stellar masses, as the NIR corresponds to the rest-frame optical at $z \sim 3$. Additional photometry across a range of wavelengths is necessary to effectively characterize SEDs and rule out drastically different natures; in particular, IRAC photometry is critical to differentiating between dust-obscured and old populations at $z > 2$. A variety of recent surveys have made such imaging available, including CANDELS (Grogin et al. 2011; Koekemoer et al. 2011), NMBS (van Dokkum et al. 2009; Whitaker et al. 2011), UltraVISTA (McCracken et al. 2012), VIDEO (Jarvis et al. 2013), DES+VHS (Banerji et al. 2015), and ZFOURGE (Straatman et al. 2016). This has resulted in an increasing number of photometric candidates that require follow-up to confirm their quiescent natures (Marchesini et al. 2010; Spitler et al. 2014; Straatman et al. 2014; Alcalde Pampiega et al. 2019; Guarnieri et al. 2019; Merlin et al. 2019; Shahidi et al. 2020).

Selection of these objects is often done using color-color diagrams (e.g., Labbé et al. 2005), the most common of which is the rest-frame ($U - V$) versus ($V - J$) plane known as the UVJ diagram (e.g., Wuyts et al. 2007; Williams et al. 2009; Martis et al. 2016; Forrest et al. 2016), where the red colors of quiescent objects make them stand out. However, at high redshifts, the clear color bimodality seen in UVJ at low redshifts is not as well defined (Whitaker et al. 2011; Muzzin et al. 2013; Straatman et al. 2016). Additionally, the presence of strong emission lines can move galaxy colors significantly, thus affecting conclusions drawn from photometry alone (e.g., Salmon et al. 2015; Forrest et al. 2018; Z. C. Marsan et al. 2020, in preparation). Spectroscopic follow-up is thus required to (1) confirm the redshift, (2) quantify the strength of emission lines associated with ongoing star formation, and (3) put limits on dust-obscured star formation.

NIR spectroscopy (corresponding to rest-frame optical wavelengths at $z \sim 3$) can inform these areas by detecting either emission features such as [O II] $\lambda\lambda 3726, 3729, H\beta \lambda 4861$, and [O III] $\lambda\lambda 4959, 5007$, or absorption features including the Balmer series and calcium H $\lambda 3970$ and K $\lambda 3935$ lines (e.g., Belli et al. 2014; Kriek et al. 2015; Belli et al. 2017; Newman et al. 2018). While the strongest constraints on dust-obscured star formation can be provided by far-infrared data, a complete lack of emission lines in a spectrum is also highly constraining. However, at $z > 3$, candidate UMGs are faint and require significant amounts of exposure time, particularly for those that do not have emission lines. Indeed, while < 20 candidate quiescent UMGs have been spectroscopically confirmed at $z > 3$ (e.g., Marsan et al. 2015, 2017; Glazebrook et al. 2017; Schreiber et al. 2018a; Tanaka et al. 2019; Forrest et al. 2020; Valentino et al. 2020; Saracco et al. 2020, submitted), only a few have been confirmed to have no emission lines, and several have far-infrared detections indicating ongoing star formation (Schreiber et al. 2018a, 2018b). All of these works have concluded that these galaxies formed their large stellar masses in short, intense bursts of star formation.

For this work, we used the H - and K -band spectroscopic capabilities of Keck-MOSFIRE (McLean et al. 2010, 2012) to follow up a set of massive candidates from XMM-VIDEO (Annunziatella et al. 2020, in preparation) and COSMOS-UltraVISTA fields (A. Muzzin et al. 2020, in preparation). The survey aimed to characterize not only quiescent candidates but also candidate UMGs in the blue star-forming region and red candidates consistent with large amounts of dust to inform the picture of galaxy formation in the early universe. We present the photometric properties and selection method in Section 2, the spectroscopic observations and data reduction in Section 3, the redshift determination and galaxy property characterization in Section 4, and then present the results in Section 5 and the main conclusions in Section 6. Throughout this work, we assume a Chabrier IMF (Chabrier 2003) and a Λ CDM cosmology with $H_0 = 70 \text{ km s}^{-1} \text{ Mpc}^{-1}$, $\Omega_M = 0.3$, and $\Omega_\Lambda = 0.7$. We also adopt an AB magnitude system (Oke & Gunn 1983).

2. Photometric Data and Target Selection

2.1. Photometric Catalogs

Massive Ancient Galaxies At $z > 3$ NEar-infrared (MAGAZ3NE) survey targets were selected from parent photometric catalogs in the UltraVISTA DR1 (Muzzin et al. 2013), UltraVISTA DR3 (A. Muzzin et al. 2020, in preparation), and XMM-VIDEO (M. Annunziatella et al. 2020, in preparation) fields.

The UltraVISTA survey McCracken et al. (2012) obtained deep near-infrared Y -, J -, H -, and K -band imaging over 1.62 deg^2 in the COSMOS field. Combined with ancillary photometry from $0.15 - 24 \mu\text{m}$, this yielded 30 bandpasses, allowing for accurate characterization of galaxy spectral energy distributions (SEDs) and precise photometric redshifts (DR1 catalogs, 90% completeness $K_s = 23.4 \text{ mag}$; Muzzin et al. 2013). Further deep imaging in the NIR yielded a set of ultra-deep strips over 0.84 deg^2 (DR3 catalogs; 90% completeness $K_s = 24.5 \text{ mag}$; Z. C. Marsan et al. 2020, in preparation; A. Muzzin et al. 2020, in preparation), which allowed for detection of massive, quiescent galaxies whose properties cannot be constrained from optical photometry alone. Considerable further photometry was also added to obtain a total of 49 bandpasses in regions where there is overlap. Critical to this work were Spitzer/IRAC mosaics using data from the S-COSMOS (Sanders et al. 2007), SPLASH (Mehta et al. 2018), and SMUVS (Ashby et al. 2018), which resulted in IRAC imaging $\sim 1.2 \text{ mag}$ deeper in the 3.6 and $4.5 \mu\text{m}$ bandpasses relative to DR1.

Similarly, the VISTA Deep Extragalactic Observations survey (VIDEO; Jarvis et al. 2013) acquired deep near-infrared Z -, Y -, J -, H -, and K_s -band imaging in three fields: the European Large Area Infrared Space Observatory S1 field, the extended Chandra Deep Field South, and the XMM-Newton Large Scale Structure (XMM) field. Of the three VIDEO fields, we only present targets from the XMM field in this work, which also has substantial photometric observations in other optical and near-infrared bandpasses. Catalogs were constructed using VIDEO DR4 data over 4.65 deg^2 with a 5σ depth of $K_s = 23.8 \text{ mag}$ (M. Annunziatella et al. 2020, in preparation). These include 22 photometric passbands ranging from u band to IRAC $8.0 \mu\text{m}$, including NIR observations from the VIDEO survey (Jarvis et al. 2013), and deep IRAC data from the SERVS (Mauduit et al. 2012) and DEEPDRILL (Lacy et al. 2020, submitted) surveys.

Table 1
Properties of UMG Candidates Derived from Fits to the Combined Spectroscopy and Photometry (see Section 4), Ordered by Stellar Mass

| UMG | z_{phot} | z_{spec} | $\log(M_{*,\text{phot}}/M_{\odot})$ | $\log(M_{*,\text{spec}}/M_{\odot})$ | $\text{SFR}_{10} (M_{\odot} \text{ yr}^{-1})$ | $t_{50} \text{ (Gyr)}$ | $t_q \text{ (Gyr)}$ | A_V |
|----------------|------------------------|------------------------------|-------------------------------------|-------------------------------------|---|------------------------|------------------------|---------------------|
| COS-DR3-202019 | $3.10^{+0.06}_{-0.04}$ | $3.1326^{+0.0021}_{-0.0011}$ | $11.52^{+0.02}_{-0.04}$ | $11.67^{+0.04}_{-0.05}$ | $82.4^{+10.4}_{-58.2}$ | $0.76^{+0.20}_{-0.05}$ | $0.40^{+0.34}_{-0.40}$ | $0.6^{+0.0}_{-0.3}$ |
| XMM-VID3-2293 | $3.07^{+0.17}_{-0.16}$ | $3.3132^{+0.0009}_{-0.0007}$ | $11.56^{+0.03}_{-0.05}$ | $11.57^{+0.02}_{-0.05}$ | $29.5^{+43.0}_{-22.3}$ | $1.12^{+0.40}_{-0.37}$ | $0.32^{+0.98}_{-0.32}$ | $0.8^{+0.2}_{-0.4}$ |
| XMM-VID1-2075 | $3.48^{+0.08}_{-0.07}$ | $3.4520^{+0.0014}_{-0.0017}$ | $11.49^{+0.02}_{-0.03}$ | $11.52^{+0.00}_{-0.05}$ | $0.0^{+1.0}_{-0.0}$ | $0.48^{+0.12}_{-0.07}$ | $0.42^{+0.12}_{-0.13}$ | $0.4^{+0.0}_{-0.2}$ |
| XMM-VID3-1120 | $3.40^{+0.12}_{-0.10}$ | $3.4919^{+0.0018}_{-0.0029}$ | $11.44^{+0.03}_{-0.04}$ | $11.47^{+0.02}_{-0.03}$ | $0.0^{+0.1}_{-0.0}$ | $0.72^{+0.10}_{-0.07}$ | $0.51^{+0.14}_{-0.22}$ | $0.0^{+0.0}_{-0.0}$ |
| COS-DR3-160748 | $3.35^{+0.02}_{-0.09}$ | $3.3524^{+0.0008}_{-0.0006}$ | $11.47^{+0.03}_{-0.03}$ | $11.46^{+0.01}_{-0.08}$ | $3.1^{+0.2}_{-0.2}$ | $0.37^{+0.10}_{-0.05}$ | $0.32^{+0.10}_{-0.05}$ | $0.0^{+0.0}_{-0.0}$ |
| COS-DR3-201999 | $3.14^{+0.09}_{-0.09}$ | $3.1313^{+0.0014}_{-0.0012}$ | $11.40^{+0.02}_{-0.05}$ | $11.40^{+0.03}_{-0.01}$ | $1.3^{+0.3}_{-1.2}$ | $0.52^{+0.10}_{-0.08}$ | $0.32^{+0.10}_{-0.05}$ | $0.4^{+0.1}_{-0.0}$ |
| COS-DR3-179370 | $3.14^{+0.72}_{-0.28}$ | $3.3673^{+0.0010}_{-0.0007}$ | $11.34^{+0.05}_{-0.02}$ | $11.37^{+0.04}_{-0.07}$ | $3.2^{+9.3}_{-2.4}$ | $1.20^{+0.10}_{-0.21}$ | $0.23^{+0.75}_{-0.14}$ | $0.8^{+0.2}_{-0.2}$ |
| COS-DR3-195616 | $3.09^{+0.09}_{-0.08}$ | $3.2552^{+0.0012}_{-0.0009}$ | $11.31^{+0.03}_{-0.03}$ | $11.31^{+0.02}_{-0.02}$ | $21.7^{+2.8}_{-12.3}$ | $0.62^{+0.15}_{-0.05}$ | $0.32^{+0.21}_{-0.05}$ | $0.6^{+0.0}_{-0.2}$ |
| COS-DR3-208070 | $3.44^{+0.06}_{-0.05}$ | $3.4912^{+0.0011}_{-0.0012}$ | $11.27^{+0.02}_{-0.10}$ | $11.26^{+0.04}_{-0.04}$ | $125^{+44.8}_{-60.5}$ | $0.30^{+0.13}_{-0.07}$ | $0.23^{+0.13}_{-0.23}$ | $1.0^{+0.1}_{-0.1}$ |
| XMM-VID3-2457 | $3.51^{+0.07}_{-0.07}$ | $3.4892^{+0.0032}_{-0.0024}$ | $11.20^{+0.03}_{-0.01}$ | $11.26^{+0.02}_{-0.03}$ | $0.0^{+0.4}_{-0.0}$ | $0.40^{+0.13}_{-0.12}$ | $0.21^{+0.10}_{-0.09}$ | $0.5^{+0.2}_{-0.1}$ |
| COS-DR3-84674 | $3.06^{+0.06}_{-0.06}$ | $3.0094^{+0.0015}_{-0.0011}$ | $11.26^{+0.02}_{-0.02}$ | $11.25^{+0.01}_{-0.01}$ | $1.1^{+0.6}_{-0.8}$ | $0.50^{+0.11}_{-0.06}$ | $0.32^{+0.14}_{-0.05}$ | $0.5^{+0.0}_{-0.1}$ |
| COS-DR1-113684 | $3.47^{+0.08}_{-0.08}$ | $3.8309^{+0.0014}_{-0.0020}$ | $11.20^{+0.04}_{-0.06}$ | $11.20^{+0.03}_{-0.04}$ | $15.7^{+0.2}_{-1.1}$ | $0.45^{+0.10}_{-0.05}$ | $0.32^{+0.11}_{-0.05}$ | $0.0^{+0.0}_{-0.1}$ |
| COS-DR3-131925 | $3.20^{+0.08}_{-0.08}$ | $3.1393^{+0.0008}_{-0.0013}$ | $11.17^{+0.04}_{-0.02}$ | $11.12^{+0.12}_{-0.05}$ | $83.9^{+152}_{-83.5}$ | $0.32^{+0.34}_{-0.15}$ | $0.05^{+0.29}_{-0.05}$ | $0.5^{+0.2}_{-0.3}$ |
| COS-DR3-226441 | $3.27^{+0.06}_{-0.06}$ | $3.2446^{+0.0014}_{-0.0012}$ | $11.34^{+0.01}_{-0.03}$ | $11.02^{+0.06}_{-0.03}$ | $10.9^{+8.8}_{-6.2}$ | $0.43^{+0.14}_{-0.06}$ | $0.32^{+0.14}_{-0.32}$ | $0.5^{+0.2}_{-0.1}$ |
| XMM-VID1-2399 | $3.68^{+0.11}_{-0.12}$ | $3.5798^{+0.0010}_{-0.0009}$ | $11.18^{+0.08}_{-0.09}$ | $11.02^{+0.14}_{-0.13}$ | $504^{+20.9}_{-50.3}$ | $0.06^{+0.23}_{-0.05}$ | $0.01^{+0.17}_{-0.01}$ | $1.8^{+0.0}_{-0.7}$ |
| COS-DR3-111740 | $3.12^{+0.05}_{-0.06}$ | $2.7988^{+0.0013}_{-0.0011}$ | $11.13^{+0.03}_{-0.04}$ | $10.98^{+0.01}_{-0.00}$ | $0.7^{+0.2}_{-0.6}$ | $0.33^{+0.10}_{-0.05}$ | $0.26^{+0.10}_{-0.07}$ | $0.0^{+0.0}_{-0.0}$ |
| COS-DR1-79837 | $3.30^{+0.19}_{-0.20}$ | ... | $11.92^{+0.06}_{-0.05}$ | ... | ... | ... | ... | ... |
| XMM-VID3-3941 | $3.04^{+0.12}_{-0.11}$ | $3.5901^{+0.0010}_{-0.0008}$ | $11.71^{+0.07}_{-0.08}$ | ... | ... | ... | ... | ... |
| XMM-VID1-2761 | $3.60^{+0.18}_{-0.17}$ | ... | $11.52^{+0.02}_{-0.03}$ | ... | ... | ... | ... | ... |
| COS-DR1-258857 | $3.27^{+0.16}_{-0.17}$ | ... | $11.31^{+0.04}_{-0.02}$ | ... | ... | ... | ... | ... |
| XMM-VID2-270 | $3.23^{+0.16}_{-0.11}$ | ... | $11.28^{+0.07}_{-0.02}$ | ... | ... | ... | ... | ... |

Note. Errors on the photometric masses assume $z = z_{\text{phot}}$. Star formation rates are taken from the best-fit SFH to the photometric and spectroscopic data, averaged over the previous 10 Myr. The formation and quenching times, t_{50} and t_q , are given as lookback times from the spectroscopic redshift. Objects whose redshift or UMG nature were not confirmed are listed at the bottom (XMM-VID3-3941 is a quasar).

2.2. Candidate UMG Targets

We selected primary targets on the basis of photometric redshift ($3 \leq z_{\text{phot}} \leq 4$; roughly the window in which $H\beta$ falls into the MOSFIRE K band) and stellar mass ($\log(M_*/M_{\odot}) > 11.0$), as fit using EAzY (Brammer et al. 2008) and FAST (Kriek et al. 2009; see Table 1). We also made a K -band magnitude cut, $m_K < 21.7$ AB. According to the MOSFIRE ETC¹⁴ a 300 minute (18 ks) exposure would allow such an object to be detected with a continuum signal-to-noise ratio (S/N) of 5/pixel, sufficient to determine a redshift from a Balmer absorption feature such as $H\beta$. In the H band, the same detection threshold corresponds to $m_H < 22.3$ AB.

In order to characterize a representative sample of UMGs at $3 < z < 4$, we aimed to observe galaxies in a variety of locations on the UVJ diagram, potentially representing different stages of massive galaxy evolution. The main goal of this survey was to obtain redshifts for UMGs, confirming that such a population exists at this epoch, and to subsequently characterize these galaxies using emission and absorption features.

Confirmation of these faint galaxies via detection of absorption lines is difficult under poor observing conditions. As such, we selected a number of UMG candidates with blue SEDs, consistent with ongoing star formation, to observe when conditions were unfavorable. These galaxies were more likely to have emission features that can more easily be detected. In particular, we considered the amount of UV flux, strength of the Lyman and Balmer breaks, UVJ colors, and photometrically derived star formation rate (SFR) for selection. While the same mass and photometric redshift thresholds applied for the

selection of these targets, the magnitude cut was relaxed half a magnitude to $m_K < 22.2$.

This selection method resulted in a sample of 33 candidate UMGs. From this sample, 21 were observed and 16 were spectroscopically confirmed. In this work, we discuss these 16 objects, but a summary of the 5 remaining objects is presented in Appendix B. Note that none of these unconfirmed objects can be ruled out as a UMG at $3 < z < 4$ —three objects had insufficient S/N to confirm a redshift, one shows a clear continuum but no defining features, and the fifth has a redshift $z = 3.6$ but hosts a luminous quasar, making its mass uncertain.

3. Observations and Data Reduction

3.1. Mask Construction and Ancillary Targets

MOSFIRE slits were arranged using the MOSFIRE Automatic GUI-based Mask Application (MAGMA) tool.¹⁵ This software requires an input list of targets with priority weighting and a range of allowable pointing positions and position angles (PA). For each candidate UMG, K -band images were visually inspected to find nearby sources that could contaminate the spectra. In several cases, PA was constrained and/or dither size altered to avoid spectral contamination. We also constructed masks ahead of time for observing in poor conditions, targeting UMG candidates more likely to show emission features as discussed above. Slit width for these masks was increased from $0''.7$ to $0''.9$.

All masks had one or two UMGs, four to eight position alignment stars, and at least one star on a science slit, for use in

¹⁴ <https://www2.keck.hawaii.edu/inst/mosfire/etc.html>

¹⁵ <https://www2.keck.hawaii.edu/inst/mosfire/magma.html>

monitoring the seeing and slit losses, as well as performing a telluric correction (see Section 3.3.2 and Appendix D). Masks were designed to include as many bright, nearby galaxies with similar photometric redshifts as possible in order to characterize the local environment via emission-line detection. Ancillary targets were prioritized based on magnitude, SED shape, z_{phot} and redshift probability distribution from EAZY, and the stellar mass and SFR fit by FAST.

3.2. Observing Plan

Bright UMG candidates with red SEDs and *UVJ* colors were prioritized for observation, as these were not expected to show strong emission features. More time and better conditions were required to confirm redshifts for these objects through the detection of absorption features. That said, classification as star-forming or quiescent via *UVJ* colors is known to not be a pure indicator of the existence or lack of emission features, as spectroscopic determination of both redshift and emission-line contamination can alter derived rest-frame colors significantly (e.g., Schreiber et al. 2018a).

We performed on-the-fly reductions throughout observing. If a UMG showed clear emission lines in the 2D reduction, we moved on to the next target for the night. However, if emission features from a UMG candidate were not clear after 2–3 hr but a stellar continuum was seen, we changed to a second mask on the same UMG. This allowed us to spectroscopically confirm neighbor galaxies to the UMG and increase the continuum S/N of the UMG for better characterization of absorption features.

Targets were initially observed with MOSFIRE *K*-band spectroscopy in order to detect any strong emission from [O III] $\lambda\lambda 4959, 5007$ and H β $\lambda 4861$ in either emission or absorption. A single exception to this was COS-DR3-84674, which was observed in the *H* band, due to concerns that a small deviation from its low z_{phot} could cause lines to fall between the *H* and *K* bands. As such, we targeted this object in the *H* band in an attempt to obtain an absorption-line redshift or detection of [O II] emission.

For half of the UMG targets, emission from [O III] $\lambda 5007$ was detected in the *K* band with S/N > 10. The remaining eight had continuum detections, but no clear emission features were seen. While in three cases the redshift could be confirmed from absorption features, the remaining five UMGs without clear spectroscopic redshifts were followed up with *H*-band spectroscopy. This allowed for detection of higher-order Balmer absorption features, CaH and CaK absorption, and the 4000 Å break, and also allowed for constraint of the spectral shape between the two bandpasses.

In total, 15 of the confirmed UMGs were observed for an average of 2 hr in the *K* band, and 6 confirmed UMGs were observed for an average of 5 hr in the *H* band. All masks were observed using an ABBA dither pattern and 180 or 120 s exposures for the *K* and *H* bands, respectively. A table of observed masks and UMG targets can be found in Appendix A.

3.3. Spectral Reduction

3.3.1. Spectral Extraction

Each mask was processed individually. In cases where a galaxy was observed on multiple masks, spectra were only stacked after each one had been processed independently and a 1D spectrum extracted. For these, the 1D spectra were coadded using inverse variance weighting based on the error spectra.

We began by running the MOSFIRE Data Reduction Pipeline (DRP),¹⁶ which constructs a pixel flat image; identifies slits; removes thermal contamination (*K* band); performs wavelength calibration using sky lines, neon arc lamps, and argon arc lamps; removes sky background; and rectifies the spectra, yielding a reduced 2D spectrum for a given mask.

While the DRP also offers an option to extract a 1D spectrum, we wrote our own custom code to perform optimal extraction (Horne 1986). Briefly, this involves collapsing the 2D spectrum for each slit along the wavelength axis and fitting a Gaussian to the summed fluxes, with a prior on the predicted position of the object on each slit. This Gaussian is then used as a weight when collapsing the spectrum along the spatial axis to obtain the 1D spectrum (and errors) for each object.¹⁷

3.3.2. Sky-line Identification and Telluric Corrections

Strong sky lines are a serious contaminant in the NIR, particularly in the *H* band, and while the DRP attempts to subtract off their flux, large flux variances remain at these locations even after subtraction. For each wavelength in a reduced mask, we calculate the median variance per pixel on sky in the spatial direction, and derive thresholds above which wavelengths are determined to be contaminated by either weak or strong sky lines. Strong sky lines are masked, while weak lines are interpolated over. More details on this process are given in Appendix C. For plotting purposes, we filled masked wavelengths by using an inverse variance-weighted average of nearby wavelengths which are not associated with sky lines.

A custom Python code was also written to perform telluric correction using stars observed in mask slits. The method is briefly described here, while a more detailed description, as well as a comparison to standard star telluric correction is provided in Appendix D. Briefly, we used the spectra of stars observed on the slits within each mask to obtain a telluric correction by fitting PHOENIX stellar models (Husser et al. 2013) to the NIR photometry of each star to obtain a model spectrum. The ratio of the model to the observed stellar spectrum was taken to be the telluric correction and was applied to all slits on a given mask. When multiple stars were observed on a mask, the resultant telluric corrections were coadded using inverse variance weighting of the spectral errors. As the subsequent fitting procedure scales the spectra to match the photometry, we were here only concerned with the correction of the spectra in terms of shape.

4. Analysis

In order to determine spectroscopic redshifts, we used a combination of the programs `slinefit`¹⁸ and FAST++¹⁹ (Schreiber et al. 2018a), a variation of the popular FAST program (Kriek et al. 2011) which fits to both photometric and spectroscopic data. FAST++ allows for different functional star formation histories (SFHs), scaling of spectra to match photometry, and fitting of spectra with different wavelength resolutions, among many other features. The program `slinefit` fits spectra with emission (and absorption) features across a range of redshifts using Gaussians of varying widths and amplitudes. In

¹⁶ <https://github.com/Mosfire-DataReductionPipeline/MosfireDRP>

¹⁷ The official MOSFIRE DRP appears to have not yet been updated to do this — <https://github.com/Keck-DataReductionPipelines/MosfireDRP/issues/126>.

¹⁸ <https://github.com/cscreib/slinefit>

¹⁹ <https://github.com/cscreib/fastpp>

this work, we are concerned with fitting [O II] $\lambda\lambda$ 3726, 3729 (line ratio fixed to unity), H β , and [O III] $\lambda\lambda$ 4959, 5007 (line ratio fixed to 0.3) for the UMGs and galaxies at similar redshifts. The program also allows for continuum fitting to enable more accurate characterization of line properties such as equivalent widths.

4.1. Fitting Photometric and Spectroscopic Data with FAST++

In fitting with FAST++, we use stellar population models from (Bruzual & Charlot 2003, BC03) with a starburst dust law (Calzetti et al. 2000). We used the following grids for various input parameters:

$$\begin{aligned} 7 < \log(\tau \text{ yr}^{-1}) < 10, \Delta\tau &= 0.1 \\ 7 < \log(\text{age yr}^{-1}) < 9.25, \Delta\text{age} &= 0.05 \\ 0 < A_V / \text{mag} < 4, \Delta A_V &= 0.1 \end{aligned}$$

In general, metallicity was fixed to $Z = 0.02 = Z_\odot$, as several studies have shown this to be broadly correct for high-redshift massive galaxies (e.g., Belli et al. 2019; Kriek et al. 2019; Estrada-Carpenter et al. 2019; Jafariyazani et al. 2020; but also see P. Saracco et al. 2020, in preparation, for a spectroscopic measurement of supersolar stellar metallicity for one of our galaxies, COS-DR3-160748). However, we did test metallicities of $0.4 Z_\odot$ and $2.5 Z_\odot$ as well, which yielded only slightly worse fits to the data and not significantly different galaxy properties.

Velocity dispersion, which must be fixed for each run of FAST++, was set to 300 km s^{-1} . While velocity dispersions of similar galaxies at these redshifts and masses are rare, Tanaka et al. (2019) calculate $\sigma = 268 \pm 59 \text{ km s}^{-1}$ for a galaxy at $z = 4.01$ with $\log(M_*/M_\odot) \sim 11$. Their Figure 4 also presents published velocity dispersions for massive quiescent galaxies at $z > 1.5$, which range from ~ 100 to $\sim 500 \text{ km s}^{-1}$ and show a slight positive correlation with stellar mass. A more in-depth analysis of velocity dispersions is beyond the scope of this work.

Characterizing the SFHs of these galaxies addresses directly the potential identification of the population from which they descended. Additionally, the maximum SFR and the time at which these galaxies quenched inform models of star formation in the young cosmos and can provide important insights into the evolution of massive galaxies in the local universe. Here we test both a delayed exponentially declining SFH²⁰ (using the parameter grid above) as well as a double-exponential SFH:

$$\text{SFR}_{\text{base}}(t) \propto \begin{cases} e^{(t_{\text{burst}} - t)/\tau_{\text{rise}}}, & \text{for } t > t_{\text{burst}} \\ e^{-(t - t_{\text{burst}})/\tau_{\text{decl}}}, & \text{for } t \leq t_{\text{burst}} \end{cases} \quad (1)$$

$$\text{SFR}(t) = \text{SFR}_{\text{base}}(t) \times \begin{cases} 1, & \text{for } t > t_{\text{free}} \\ R_{\text{SFR}}, & \text{for } t \leq t_{\text{free}} \end{cases} \quad (2)$$

This SFH has been used in other works studying massive galaxies at high redshift (Schreiber et al. 2018a; Forrest et al. 2020; Valentino et al. 2020), and we adopt the same parameter

²⁰ $\text{SFR}(t) \propto te^{-t/\tau}$.

grid described therein:

$$\begin{aligned} 7.0 < \log(t_{\text{burst}} \text{ yr}^{-1}) < 9.2, \Delta \log(t_{\text{burst}} \text{ yr}^{-1}) &= 0.05 \\ 7.0 < \log(\tau_{\text{rise}} \text{ yr}^{-1}) < 9.5, \Delta \log(\tau_{\text{rise}} \text{ yr}^{-1}) &= 0.1 \\ 7 < \log(\tau_{\text{decl}} \text{ yr}^{-1}) < 9.5, \Delta \log(\tau_{\text{decl}} \text{ yr}^{-1}) &= 0.1 \\ 7 < \log(t_{\text{free}} \text{ yr}^{-1}) < 8.5, \Delta \log(t_{\text{free}} \text{ yr}^{-1}) &= 0.5 \\ -2.0 < \log(R_{\text{SFR}}) < 5.0, \Delta \log(R_{\text{SFR}}) &= 0.2 \end{aligned}$$

We emphasize that while the exact shape of the best-fit SFH is model dependent and can vary depending upon assumptions of the parametric form, general characteristics, such as when the majority of stars were formed and when the galaxy quenched, can be well constrained provided that the SFH inputs are sufficiently flexible and appropriate for the object in question. In particular, Belli et al. (2019) show that various SFH parameterizations yield similar values of star-forming timescale and sSFR. We find the same for the delayed- τ and double-exponential models described here, and we will use values from the double-exponential fits in the remainder of the work.

4.2. Redshift Determination and Template Fitting for Absorption-line UMGs

When stellar continuum is detected with no clear emission features, we use FAST++ to determine the redshift. For galaxies with spectra in both the H and K bands, we fit the spectrum of each band combined with the photometry independently in order to remove differences in flux scaling between the spectra when matching the photometry. The two spectra are then scaled relative to each other and refit in combination with the photometry. This relative rescaling between bands can be up to 15% depending on the accuracy of the flux calibration factor in the slit star telluric correction.

For redshift fitting, we fit to the combined photometry and spectroscopy of the galaxy in question. We do three runs per galaxy, the first with the model redshifts in the range $2.5 < z_{\text{model}} < 4.0$ with $\Delta z = 0.01$ to obtain an initial fit, $z_{\text{spec},0}$, and a second run with model redshifts $z_{\text{spec},0} - 0.02 < z_{\text{model}} < z_{\text{spec},0} + 0.02$ and $\Delta z = 0.0001$ to obtain a final z_{spec} . While these two runs are completed with a delayed- τ SFH, the third run uses a double-exponential SFH with the possibility of additional low levels of late-time star formation (see Section 4.1 as well as Schreiber et al. 2018b, 2018a). This SFH is more computationally intensive and thus having the redshift fixed to z_{spec} improves runtime significantly. More details on the fitting input parameters are given in Section 4.1.

We subsequently run `slinefit` on the spectrum, with the best-fit model from FAST++ used as the stellar continuum template. This allows for measurement or limits on the strength of weak emission features in these galaxies. This does not affect the redshift determination at all, only the line measurements. Final line fluxes and equivalent widths are presented in Table 2.

4.3. Redshift Determination and Template Fitting for Emission-line UMGs

For galaxies where emission features are detected we use `slinefit` to determine the spectroscopic redshift, z_{spec} . In this first fit we use a set of high resolution galaxy spectral templates based on those provided in EAzy (Brammer et al. 2008) to

Table 2
Properties of Confirmed UMGs Derived from Fits to the Spectra. Fluxes Are in Units of 10^{-18} erg s $^{-1}$ cm $^{-2}$

| UMG | $f_{\text{[OII]}}$ | $EW_0(\text{[O II]})$ | $\text{SFR}_{\text{[OII]}}$ | $D_n(4000)$ | $EW_0(\text{H}\delta)$ | $f_{\text{H}\beta}$ | $EW_0(\text{H}\beta)$ | $\text{SFR}_{\text{H}\beta}^{\text{a}}$ | $f_{\text{[OIII]}\lambda 4959}$ | $EW_0(\text{[O III]}\lambda 4959)$ | $f_{\text{[OIII]}\lambda 5007}$ | $EW_0(\text{[O III]}\lambda 5007)$ |
|-----------------------------|--------------------|-----------------------|-----------------------------|-----------------|------------------------|---------------------|-----------------------|---|---------------------------------|------------------------------------|---------------------------------|------------------------------------|
| COS-DR3-202019 | 162 ± 7 | -30.1 ± 3.4 | 57.6 ± 2.6 | 1.15 ± 0.10 | 8.3 ± 1.7 | 32.0 ± 11.6 | -6.5 ± 2.4 | 36.5 ± 13.3 | 9.9 ± 2.4 | -2.0 ± 0.5 | 33.2 ± 7.9 | -6.7 ± 1.6 |
| XMM-VID3-2293 ^b | ... | ... | ... | ... | ... | 44.3 ± 6.9 | -19.3 ± 3.3 | 57.9 ± 9.1 | 95.8 ± 2.0 | -40.8 ± 3.0 | 320 ± 7 | -136 ± 10 |
| XMM-VID1-2075 | ... | ... | ... | ... | ... | 6.3 ± 1.5 | -1.4 ± 0.3 | 9.1 ± 2.2 | 1.2 ± 1.5 | -0.3 ± 0.3 | 4.0 ± 4.9 | -0.9 ± 1.1 |
| XMM-VID3-1120 | 6.0 ± 5.0 | -1.4 ± 1.2 | 2.8 ± 2.3 | ... | ... | 2.8 ± 3.3 | -1.5 ± 0.9 | 4.2 ± 4.9 | -4.4 ± 1.2 | 1.1 ± 0.3 | -14.6 ± 4.1 | 3.8 ± 1.1 |
| COS-DR3-160748 ^b | ... | ... | ... | ... | ... | 17.8 ± 7.2 | -5.7 ± 0.9 | 23.9 ± 9.7 | 47.6 ± 2.1 | -5.9 ± 0.3 | 158.7 ± 7.1 | -19.8 ± 1.0 |
| COS-DR3-201999 ^b | 17.8 ± 3.5 | -4.2 ± 0.9 | 6.3 ± 1.2 | 1.21 ± 0.05 | 9.1 ± 0.8 | 1.3 ± 2.2 | -0.3 ± 2.6 | 1.5 ± 2.5 | 3.4 ± 1.0 | -0.8 ± 0.2 | 11.3 ± 3.2 | -2.8 ± 0.8 |
| COS-DR3-179370 | ... | ... | ... | ... | ... | 10.8 ± 3.5 | -8.8 ± 2.9 | 14.6 ± 4.7 | 19.2 ± 0.7 | -15.5 ± 1.1 | 64.0 ± 2.2 | -51.6 ± 3.5 |
| COS-DR3-195616 ^b | ... | ... | ... | ... | ... | 12.4 ± 2.2 | -5.5 ± 1.0 | 15.5 ± 2.8 | 23.1 ± 1.3 | -10.0 ± 0.7 | 77.1 ± 4.5 | -33.4 ± 2.3 |
| COS-DR3-208070 | ... | ... | ... | ... | ... | 32.3 ± 2.8 | -15.6 ± 1.4 | 47.8 ± 4.1 | 12.4 ± 0.6 | -5.8 ± 0.3 | 41.5 ± 2.1 | -19.4 ± 1.2 |
| XMM-VID3-2457 | 5.3 ± 4.1 | -2.0 ± 1.6 | 2.5 ± 1.9 | ... | ... | 1.5 ± 2.6 | -0.6 ± 1.1 | 2.2 ± 3.8 | 3.1 ± 1.0 | -1.3 ± 0.4 | 10.5 ± 3.3 | -4.3 ± 1.4 |
| COS-DR3-84674 | 6.2 ± 2.1 | -2.0 ± 3.6 | 2.0 ± 0.7 | 1.47 ± 0.06 | 7.2 ± 0.7 | ... | ... | ... | ... | ... | ... | ... |
| COS-DR1-113684 | ... | ... | ... | ... | ... | 4.8 ± 2.1 | ... | ... | ... | ... | ... | ... |
| COS-DR3-131925 ^b | ... | ... | ... | ... | ... | 76.5 ± 52.6 | -19.4 ± 17.0 | 87.8 ± 60.3 | 156 ± 12 | -38.9 ± 12.9 | 518 ± 40 | -130 ± 43 |
| COS-DR3-226441 ^b | ... | ... | ... | ... | ... | 50.8 ± 6.5 | -29.7 ± 5.7 | 63.1 ± 8.0 | 116 ± 2 | -65.7 ± 7.2 | 386.8 ± 7.8 | -219.1 ± 24.1 |
| XMM-VID1-2399 ^b | ... | ... | ... | ... | ... | 0.4 ± 4.4 | -0.3 ± 2.9 | 0.7 ± 7.0 | 21.5 ± 2.0 | -13.7 ± 1.6 | 71.8 ± 6.6 | -45.6 ± 5.2 |
| COS-DR3-111740 | ... | ... | ... | 1.10 ± 0.03 | 11.4 ± 0.5 | ... | ... | ... | ... | ... | ... | ... |

Notes. Equivalent widths are in rest-frame Ångstroms and in the case of H β is calculated after taking stellar continuum absorption into account. Negative values indicate emission.

^a. This calculation assumes all flux from the line is due to star formation. This may be considered an upper limit for those galaxies that host AGNs.

^b. $f_{\text{[OIII]}\lambda 5007}/f_{\text{H}\beta} > 6$, consistent with AGNs at these large stellar masses.

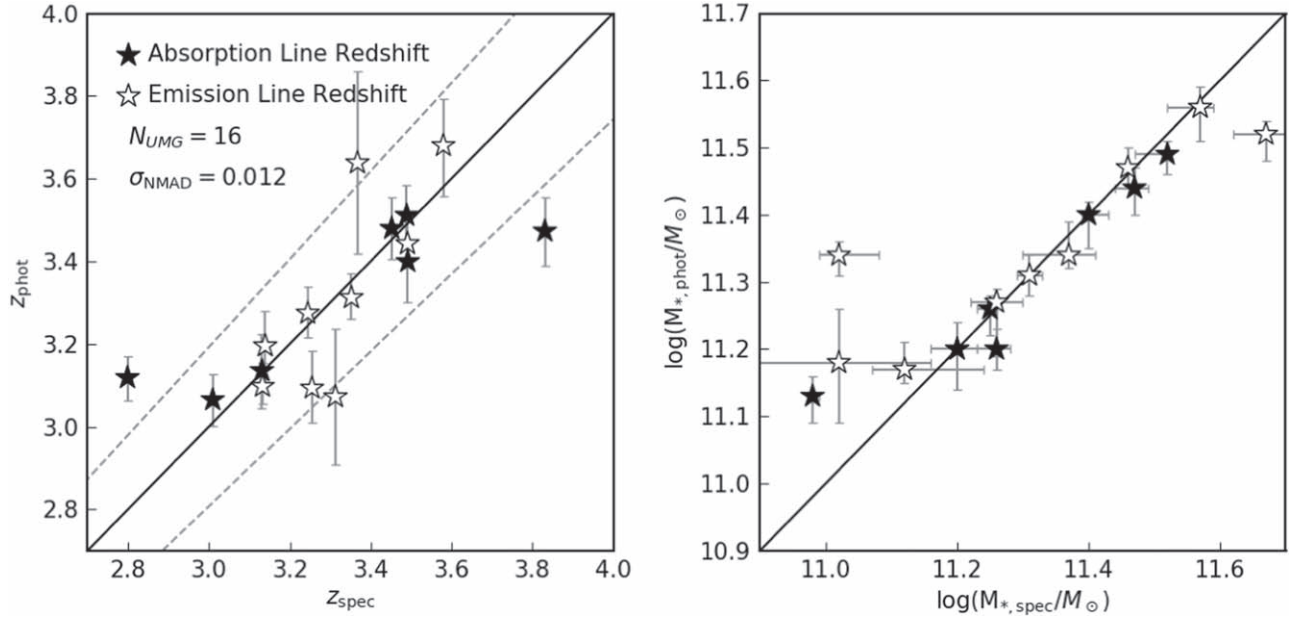


Figure 1. Comparison of photometric and spectroscopic redshifts (left) and masses (right) for confirmed UMGs. Those with detected emission lines are shown as white stars, while UMGs confirmed via absorption features are in black. The black 1:1 line on the left is bounded by two dashed lines at $5\sigma_{\text{NMAD}}$. Errors on z_{spec} are smaller than the marker size. See Table 1 for numbers.

generate a stellar continuum on top of which to fit lines. The resultant z_{spec} is then fixed when fitting with FAST++.

Before fitting these galaxies with FAST++ however, we must correct the observed photometry for the effects of the emission lines, as the template libraries do not include them. To do this, the observed magnitude is converted to a total flux by multiplying the average flux density by the width of the bandpass. In the K -band, the photometric flux is reduced by the sum of the emission-line fluxes,

$$F_{K,\text{corr}} = F_{K,\text{obs}} - (F_{\text{H}\beta} + F_{[\text{O III}]\lambda 4959} + F_{[\text{O III}]\lambda 5007}) \quad (3)$$

where the line fluxes are taken from the model output of `slinefit`.

In most cases, we do not have H -band spectra, and so we must estimate the effects of photometric contamination by [O II]. We do this by making the following assumptions:

(1) the [O II] line flux is due to a combination of star formation and active galactic nucleus (AGN) activity,

$$F_{[\text{O II}],\text{total}} = F_{[\text{O II}],\text{SFR}} + F_{[\text{O II}],\text{AGN}} \quad (4)$$

(2) case B recombination can be used to obtain an SFR from $\text{H}\beta$ (Kennicutt 1998; Moustakas et al. 2006),

$$\text{SFR}_{\text{H}\alpha} = 4.65 \times 10^{-42} L_{\text{H}\alpha} \quad (5)$$

$$L_{\text{H}\alpha} = 2.86 L_{\text{H}\beta} \quad (6)$$

$$\text{SFR}_{\text{H}\beta} = 1.33 \times 10^{-41} L_{\text{H}\beta}, \quad (7)$$

where L_i is in units of erg s^{-1} and SFRs are in units of $M_{\odot} \text{ yr}^{-1}$.

(3) the SFR derived from $\text{H}\beta$ is equal to that derived from [O II],

$$\text{SFR}_{\text{H}\beta} = \text{SFR}_{[\text{O II}]} \quad (8)$$

$$\text{SFR}_{[\text{O II}]} = 4.14 \times 10^{-42} L_{[\text{O II}],\text{SFR}} \quad (9)$$

(4) the ratio of [O III] $\lambda 5007$ to [O II] due to AGN activity is given by typical values (Silverman et al. 2009):

$$L_{[\text{O II}],\text{AGN}}/L_{[\text{O III}]\lambda 5007,\text{AGN}} = 0.21 \quad (10)$$

Tying all these pieces together leaves us with an [O II] line flux estimation as a function of the $\text{H}\beta$ and [O III] $\lambda 5007$ line fluxes observed in the K -band spectra. Equation (4) then becomes

$$F_{[\text{O II}],\text{total}} = 3.21 F_{\text{H}\beta} + 0.21 F_{[\text{O III}]\lambda 5007} \quad (11)$$

and we can correct the H -band photometry accordingly:

$$F_{H,\text{corr}} = F_{H,\text{obs}} - F_{[\text{O II}]} \quad (12)$$

We note that while the various assumptions made in these calculations may not be accurate in every case, the typical effect of the H -band photometric correction is only a few percent, and a factor of 2 in the correction does not change the resultant best-fit parameters for the equations significantly, particularly because the spectroscopic redshift is known. Furthermore, any effects of dust would only decrease the strength of [O II] relative to $\text{H}\beta$ and [O III], and thus any correction would be smaller than calculated here.

Next we use FAST++ to fit the galaxy with the redshift fixed to that obtained with `slinefit`. For this process, we input the corrected photometry, as well as spectra with the emission-line regions masked, again due to the fact that the template libraries in use do not include emission features. As above, galaxies with spectra in both the H and K bands are fit with each spectral band independently and then scaled to match the entire spectrum. Once a best-fit template is obtained from FAST++, we then repeat the entire process, i.e., we rerun `slinefit` with the best-fit FAST++ template input as the continuum model, use the resulting revised line strength estimates to recorrect the photometry, and refit with FAST++. In all cases, the new line flux and equivalent-width values are similar to the initial values, with differences of $<15\%$.

The spectroscopic and photometric redshifts agree quite well (see Figure 1 and Table 1), with $\sigma_{\text{NMAD}} = 0.012$ for the UMGs.

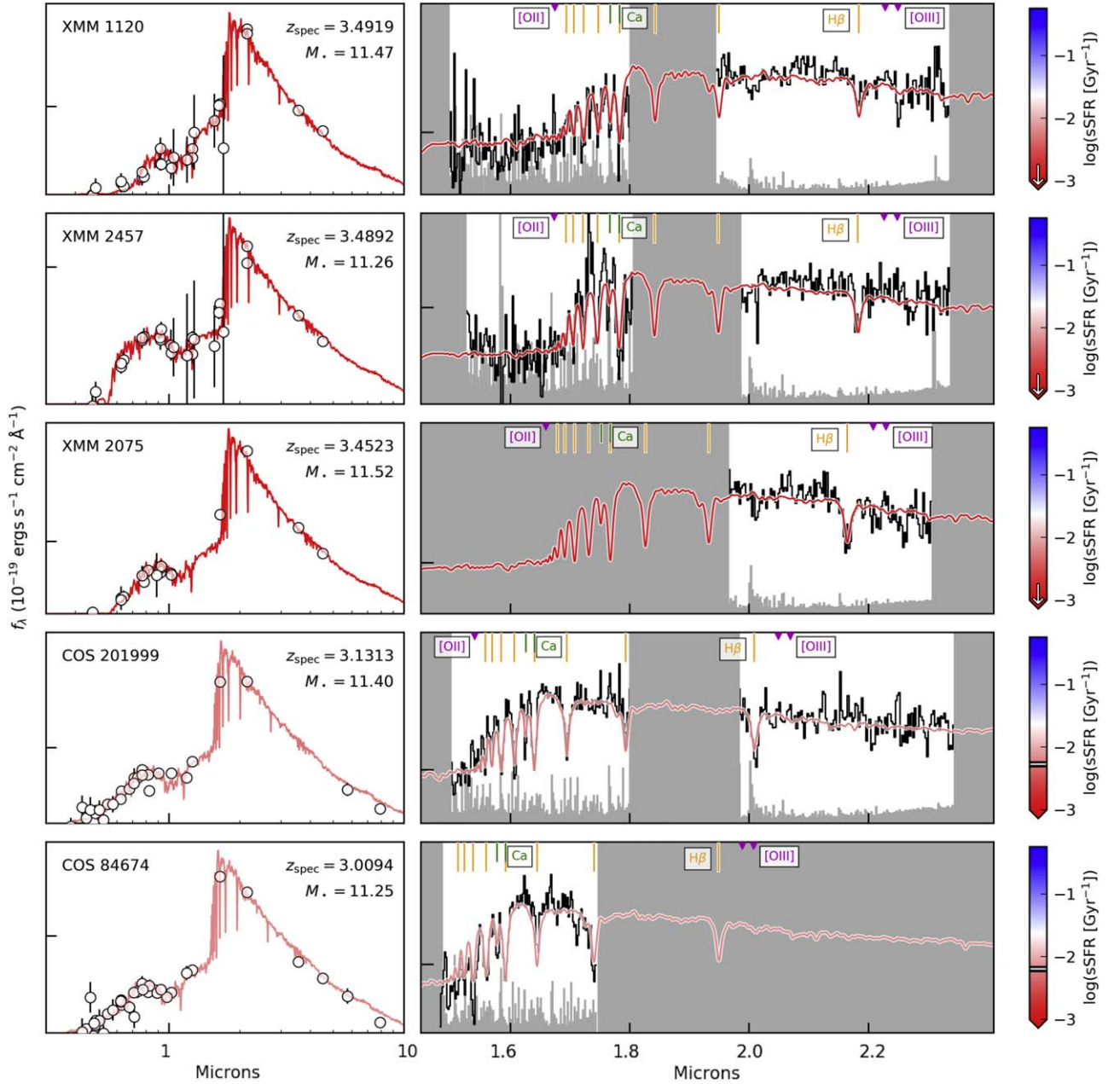


Figure 2. The photometry (left) and spectroscopy (right) for each spectroscopically confirmed UMG. The best-fit template to the combined photometry and spectroscopy is shown colored by the template’s sSFR averaged over the last 10Myr, which is indicated by a black and white line/arrow on the color bar to the right. Spectra are plotted in bins of 12 pixels, weighted by inverse variance, with errors shown in gray. Wavelengths corresponding to prominent spectral features from hydrogen (orange), oxygen (magenta), and calcium (green) are also labeled. The dash on each y-axis corresponds to a flux density of 5×10^{-19} ergs s^{-1} cm^{-2} \AA^{-1} .

As defined in Brammer et al. (2008),

$$\sigma_{\text{NMAD}} = 1.48 \times \text{median} \left(\left| \frac{\Delta z - \text{median}(\Delta z)}{1 + z_{\text{spec}}} \right| \right)$$

Similarly, the final stellar masses agree very well with those derived from the photometric catalogs alone. The largest discrepancies occur for galaxies with strong emission-line contamination and one with a large redshift discrepancy. Best-fit spectral models are shown plotted with the observed

photometry and spectra in Figures 2, 3, and 4. These figures also show the line fits and effects of photometric corrections for line emission.

5. Results

5.1. Absorption-line Galaxies

Of the 16 confirmed UMGs in the sample, 7 show well-detected absorption features and lack emission features. Five of these absorption-line galaxies are *UVJ* quiescent residing in the lower region of the quiescent wedge typically associated with young post-starburst galaxies. Notably, XMM-VID3-1120 was

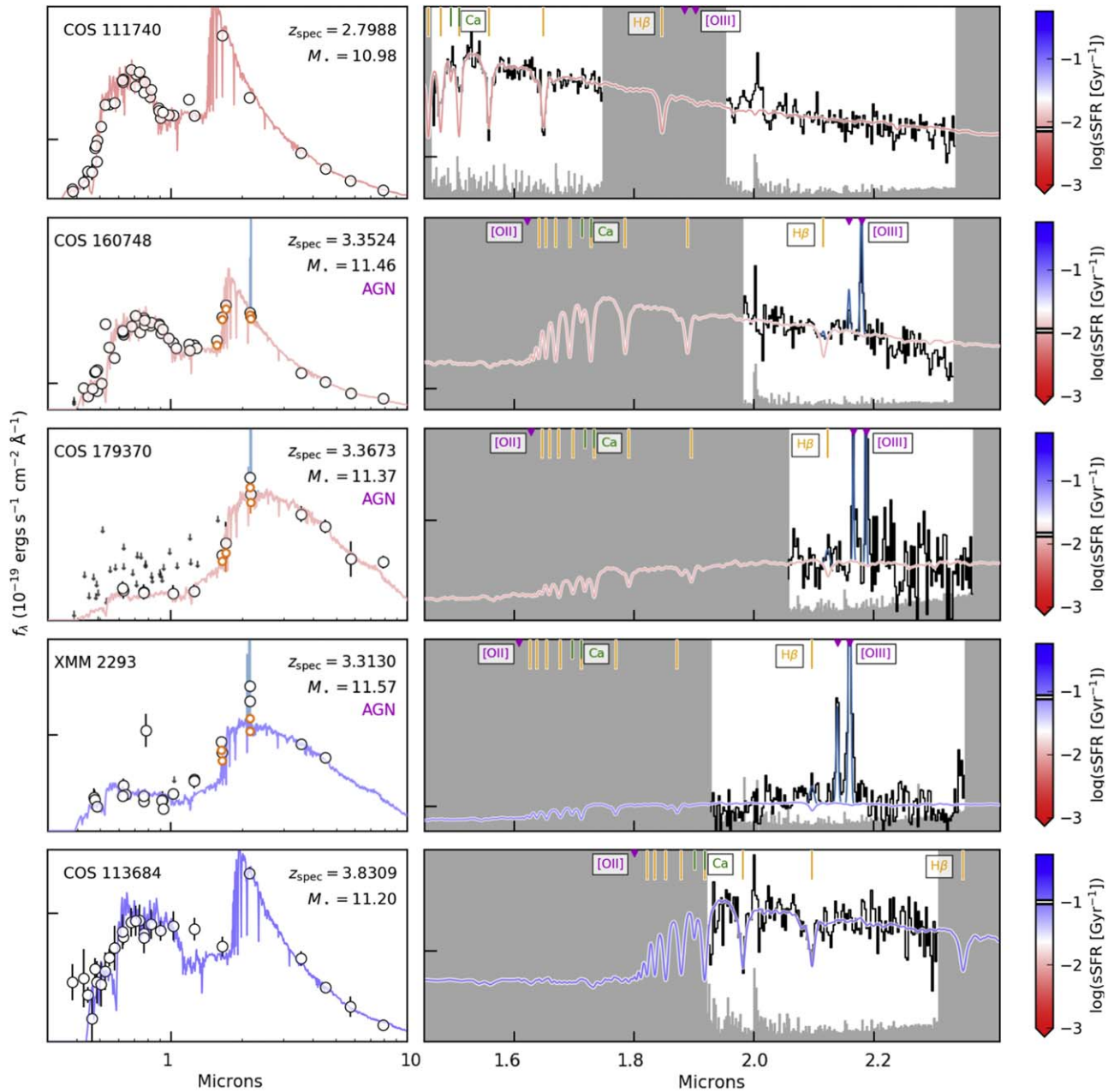


Figure 3. Same as Figure 2. For UMGs with strongly detected emission features, the best-fit model to the observed emission lines is overlaid in teal. Orange points indicate the photometry corrected for the flux of emission lines (see Section 4.3), while photometric points with $S/N < 3$ are shown as downward-facing arrows.

published in Forrest et al. (2020) as XMM-2599—the updated identifier is due to a new catalog version.

The remaining two absorption-line galaxies (COS-DR3-111740, $z = 2.80$, and COS-DR1-113684, $z = 3.83$) are at redshifts where a combination of the wavelength coverage of MOSFIRE, position of the object on the chip, and the bandpasses observed do not allow access to the [O II], $H\beta$, or [O III] emission features, and as such, emission features could be present. This also results from the spectroscopic redshifts of these two objects being discrepant from their photometric redshifts—indeed, they are clear outliers on Figure 1. Both have similar UVJ colors and SEDs to COS-DR3-160748 (discussed below), consistent with galaxies that have very

recently ceased forming new stars or have small residual amounts of star formation.

5.2. Emission-line Galaxies

The remaining nine UMGs show clear emission features with $S/N > 10$ from [O II] or [O III] $\lambda 5007$. Of these, seven have a line ratio $f_{[O\ III]\lambda 5007}/f_{H\beta} > 6$ (labeled in Table 2 and Figures 2, 3, 4), which is typically associated with AGN activity, especially at high mass (e.g., Baldwin et al. 1981; Juneau et al. 2011; Kewley et al. 2013; Trump et al. 2013; Shapley et al. 2015; Strom et al. 2017; Reddy et al. 2018). This agrees with numerous previous studies that suggest that AGN

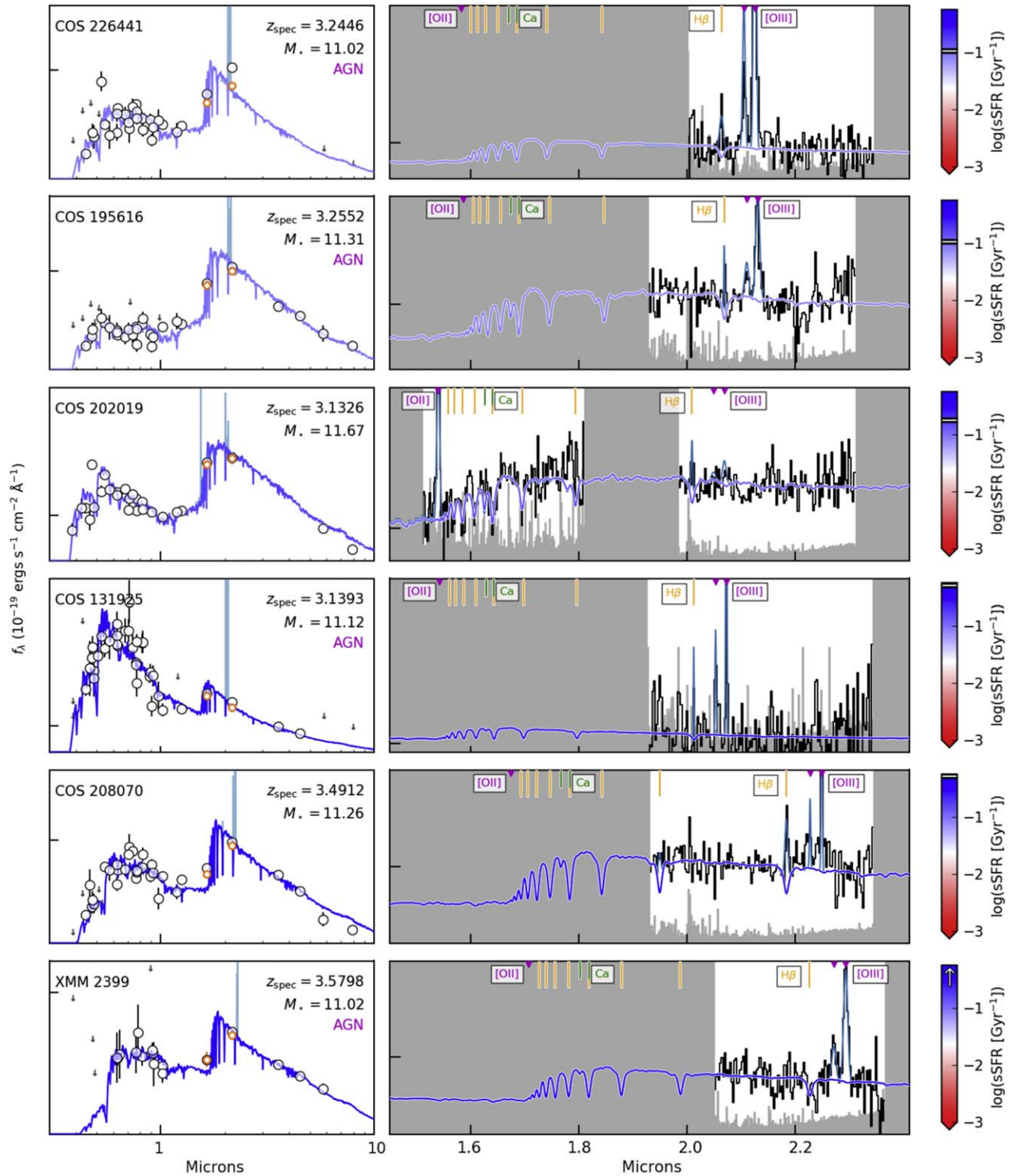


Figure 4. Same as Figures 2 and 3.

activity is more common at high redshifts (e.g., Marsan et al. 2017), though this is the largest spectroscopic sample of this mass and redshift to be analyzed.

One of these, COS-DR3-160748, was first spectroscopically confirmed in Marsan et al. (2015), and a deep spectrum has recently been analyzed in Saracco et al. (2020, submitted). Stellar masses derived in all three works are in rough agreement ($11.3 < \log(M_*/M_\odot) < 11.5$), as are the conclusions that an AGN exists in this galaxy and there is little ongoing star formation.

5.3. Rest-frame Colors

Figure 5 shows the spectroscopically confirmed galaxies on the rest-frame UVJ color-color diagram, which has been well used as a discriminator between star-forming and quiescent galaxies (e.g., Labbé et al. 2006; Williams et al. 2009; Forrest et al. 2018; Schreiber et al. 2018a). However, at high redshifts, the clear bimodality in colors between these populations appears to erode, no longer providing a selection as pure as at lower redshifts (e.g.,

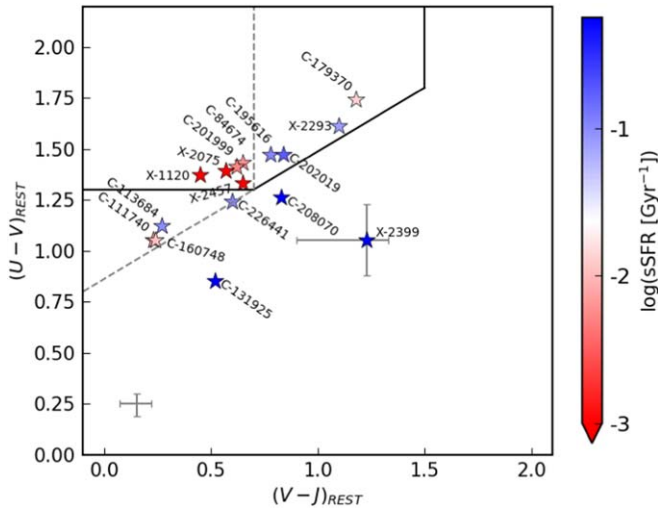


Figure 5. The rest-frame UVJ diagram for all confirmed UMGs, colored by $sSFR$ averaged over the last 10 Myr based on the best-fit SFH. The median error bar is shown in the lower left, and the only UMG with an error bar twice this size has the error plotted on the point.

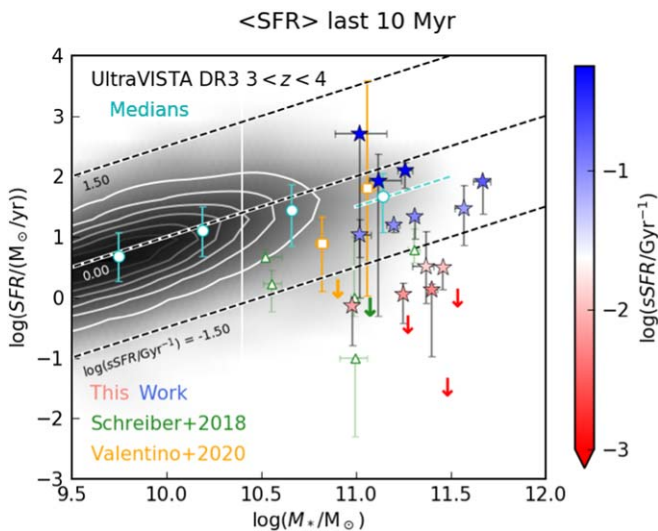


Figure 6. The SFR–stellar-mass plane. UMGs are shown as stars with the same color scheme as in previous figures. The population of galaxies at $3 < z < 4$ in the UltraVISTA DR3 catalog is shown in black, with the stellar-mass completeness limit of the catalog as a white vertical line and medians in bins of 0.5 dex in stellar mass also shown in cyan. The highest mass bin average corresponds to $\log(sSFR/\text{Gyr}^{-1}) \sim -0.5$, which is represented by a dashed cyan line spanning the width of the bin. Massive $z > 3$ galaxies from Schreiber et al. (2018a) and Valentino et al. (2020) are shown in green and orange, respectively.

Whitaker et al. 2011; Muzzin et al. 2013; Straatman et al. 2016). Part of the reason for this is that galaxies can be passive for up to several hundred megayears (depending on SFH) before their colors reach the quiescent wedge on the UVJ diagram (Merlin et al. 2018). While this is a short time relative to the lifetime of local galaxies, it is non-negligible in the high-redshift universe and thus one would expect a larger fraction of galaxies to be observed in such a phase.

Schreiber et al. (2018a) suggest simply extending the diagonal wedge line to bluer colors for samples of massive galaxies, though they then encounter some star-forming

contaminants in the resulting selection. We add this extension in Figure 5 and find that three additional UMGs are included in the resulting quiescent wedge. All have SEDs with small amounts of UV flux, consistent with low levels of star formation as would be expected in a galaxy that has recently undergone a starburst event and is now quenching its star formation, as well as a very blue $(V - J)$, indicating the lack of an older, passive stellar population.

Three galaxies with strongly detected emission lines are also UVJ quiescent, even when accounting for the effects of their emission features. Two of these have large $[\text{O III}]\lambda 5007/\text{H}\beta$ ratios, implying that their emission lines are due to AGN activity and not ongoing star formation, while the third has clear $[\text{O II}]$ emission and negligible $[\text{O III}]$, suggestive of some ongoing star formation. We thus conclude that the standard UVJ diagram, while still doing a decent job of separating star-forming and quiescent galaxies, provides neither a complete nor pure selection of either population at this mass and redshift regime.

5.4. Star Formation Rates

We compare the UMGs on the SFR versus stellar-mass plane to other $3 < z < 4$ galaxies in the UltraVISTA DR3 catalogs (Muzzin et al. 2020, in preparation), for which the SFRs and stellar masses were calculated using an exponentially declining SFH (Figure 6). All SFRs plotted here are averages over the last 10 Myr as calculated from each galaxy’s best-fit SFH. Using the instantaneous SFR or averaging over 100 Myr does not make any significant difference to our conclusions. The absorption-line UMGs fall at least one dex below the star-forming main sequence (SFMS), clearly consistent with galaxies having highly inhibited, if not completely quenched, star formation. This is also the case for several other massive $z > 3$ galaxies from Schreiber et al. (2018a). The confirmed emission-line galaxies are generally consistent with the SFMS, though they average only $\log(sSFR [\text{Gyr}^{-1}]) \sim -1$, or $\text{SFR} \sim 15 M_{\odot} \text{yr}^{-1}$.

In addition to the SFRs derived from the emission-line-corrected photometry and masked spectroscopy, we also derive SFRs from $\text{H}\beta$ and $[\text{O II}]$ lines when observed in the spectra, providing other probes of star formation. Comparing the results of these star formation indicators is important in assessing their accuracy, and we show this in Figure 7. Though these probes do measure star formation over slightly different timescales, agreement between various measurements for individual galaxies is quite good. In logarithmic space, the differences are most significant for low $sSFR$, but differences in absolute terms here are on the order of $\Delta \text{SFR} \sim 1 M_{\odot} \text{yr}^{-1}$.

5.5. Stellar Ages

The spectral indices $D_n(4000)$ and $EW_0(\text{H}\delta)$ (Balogh et al. 1999) combine to form an effective probe of stellar age that breaks a degeneracy with metallicity (e.g., Kauffmann et al. 2003). In the local universe, massive galaxies tend to show larger $D_n(4000)$ and lower $EW_0(\text{H}\delta)$, as they quenched long ago, while less massive galaxies, on average containing younger stellar populations have lower $D_n(4000)$ and higher $EW_0(\text{H}\delta)$.

We are able to measure both spectral features for four of the UMGs and use published values for a fifth using spectra from LBT/LUCI in Saracco et al. (2020, submitted). The spectral wavelength coverage of the other UMGs does not allow for one or both measurements due to different redshifts and bandpasses

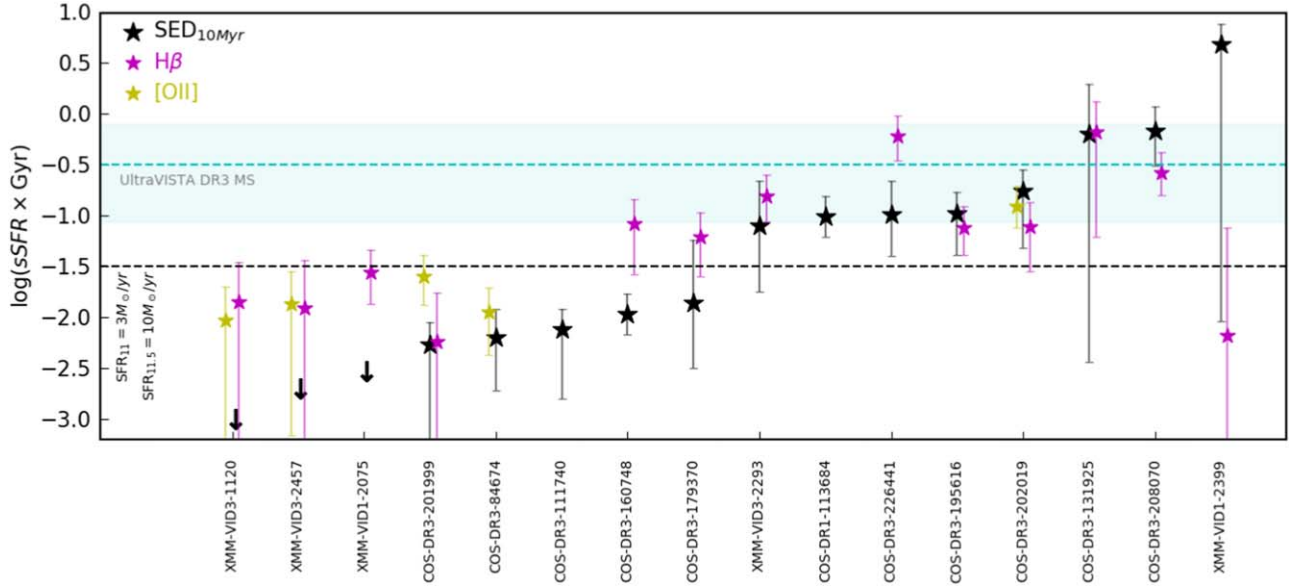


Figure 7. Comparison of sSFR for the UMGs using various star formation indicators. Black stars show the SFH from the best-fit template averaged over 10 Myr, gold stars use SFR from the [O II] line, and magenta stars use SFR from the $H\beta$ line. Note that the $H\beta$ value assumes all line flux is from star formation, which is not accurate for AGN hosts and may therefore be an upper limit. The sSFR from the massive bin of the DR3 catalog plotted in Figure 6 is shown in cyan. An sSFR 1 dex below this value, corresponding to $SFR = 3 M_{\odot} \text{yr}^{-1}$ for a $\log(M_*/M_{\odot}) = 11$ UMG, and $SFR = 10 M_{\odot} \text{yr}^{-1}$ for a $\log(M_*/M_{\odot}) = 11.5$ UMG, is shown as a black dashed line.

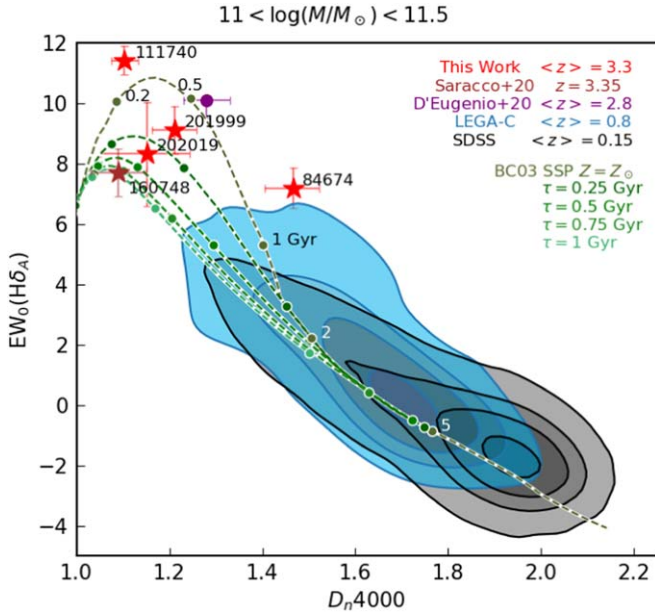


Figure 8. The $EW_0(H\delta) - D_n(4000)$ plane, used to constrain age. Lower-redshift samples from SDSS and LEGA-C, presented in Wu et al. (2018), are shown in black and blue, respectively. A stack of nine galaxies from D’Eugenio et al. (2020) is shown in purple. The UMGs with spectroscopic coverage of both features are shown in red, while COS-160748, presented in P. Saracco et al. (2020, in preparation), is shown in brown. Stellar evolution tracks for a simple stellar population (SSP) and exponentially declining SFH with varying τ are shown in shades of green. Ages of 0.2, 0.5, 1, 2, and 5 Gyr are marked with a circle for each track.

observed. These are shown in Figure 8, along with large samples of massive galaxies at $z \sim 0.1$ and $z \sim 0.8$ published in Wu et al. (2018). Also plotted is a stack of massive galaxies at $z \sim 2.8$ from D’Eugenio et al. (2020). Taken together, these data paint a picture showing that the most-massive galaxies at high redshifts are younger than galaxies of similar mass at lower redshifts. This makes sense due to the younger age of the

universe, as well as numerous studies suggesting that high-mass galaxies appear to have formed much of their stellar mass at earlier times than lower-mass galaxies at a given epoch (e.g., Pacifici et al. 2016; Bellstedt et al. 2020). Indeed, when compared to various evolutionary tracks, the UMGs are consistent with stellar ages of 200–800 Myr.

5.6. Star Formation Histories

These ages can be compared to the ages determined from the best-fit SFHs of the modeling. As a reminder, we use FAST++ to simultaneously fit the photometry and spectroscopy, and thereby derive the formation lookback time, by which point half of the observed stellar mass has been formed, and the quenching lookback time, at which time star formation in a galaxy has fallen below 10% of the average during the main burst of star formation (Table 1). While a double-exponential SFH parameterization is used, conclusions do not change if a delayed-exponential profile is used instead (see Section 4.1).

Using this methodology, the resulting best-fit SFHs show short (median timescale of 120 Myr), intense (median of $1500 M_{\odot} \text{yr}^{-1}$) bursts of star formation responsible for the vast majority of stellar-mass growth. These bursts occurred $320 < t_{50}/\text{Myr} < 740$ in the past, consistent with the ages surmised from spectral indices above. Following this, star formation rates truncated quickly. UMG quenching times are narrowly constrained to lookback times of $240 < t_q/\text{Myr} < 510$ for those UMGs no longer forming stars, and the median value is 310 Myr (Figure 9). This quenching happens rapidly with median timescale $t_{50} - t_q = 180$ Myr. The derived timescales are in good agreement with those from Saracco et al. (2020), who performed an independent analysis on deeper $H + K$ spectra for COS-DR3-160748.

5.6.1. Rapidly Star-forming Progenitors

The confirmation of a number of highly dust-obscured massive star-forming galaxies at $z > 5$ (Capak et al. 2011; Riechers et al. 2013; Ma et al. 2015; Riechers et al. 2017;

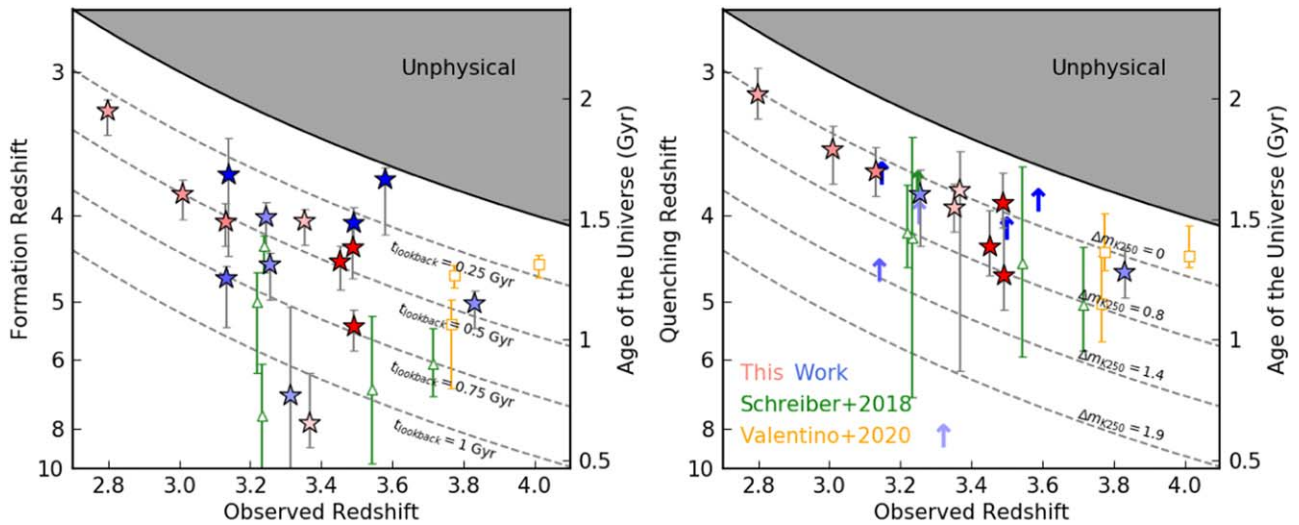


Figure 9. The evolution of spectroscopically confirmed UMGs. As previously, the sample from this work is shown colored by sSFR, galaxies from Schreiber et al. (2018a) are green, and those from Valentino et al. (2020) are orange. Left: the redshift at which the galaxy had formed 50% of its stellar mass, as determined from the best-fit SFH. The dashed lines indicate lookback time in intervals of 250 Myr. Right: the redshift at which the SFR fell below 10% of its average during the main starburst period. Upward arrows indicate UMGs that are consistent with still forming stars above this threshold. The difference in K -band magnitude a galaxy would present due to quenching at a lookback time greater than 250 Myr (Δm_{K250}) is shown on each dashed line (see also Figure 11 and Appendix E). This assumes an SFH consisting of a period of constant star formation for 100 Myr, followed by an exponentially declining SFR with $\tau = 100$ Myr, as well as no dust attenuation.

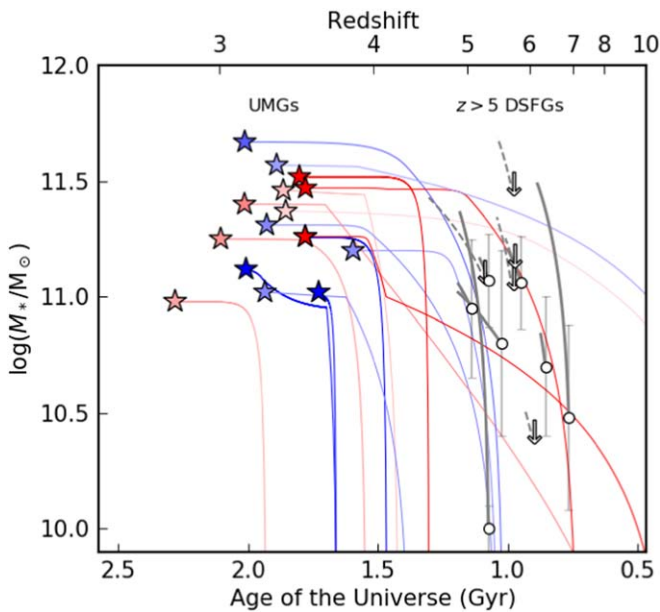


Figure 10. The stellar-mass evolution of spectroscopically confirmed UMGs according to their best-fit SFHs. A set of spectroscopically confirmed DSFGs at higher redshifts is shown in gray. The tracks on this population correspond to the growth assuming the observed SFR continuing for half of the depletion timescale, i.e., consuming half the available gas to produce stars.

Strandet et al. 2017; Marrone et al. 2018; Pavese et al. 2018; Zavala et al. 2018; Jin et al. 2019) has raised the question of how these galaxies evolve and what their descendants look like. Naturally, massive quiescent galaxies must be an eventual evolutionary stage, as these galaxies cannot continue forming stars at the observed rates for more than several hundred megayears (assuming no large inflows of cool gas to use as fuel). The idea that such galaxies might be the progenitors of lower-redshift massive quiescent galaxies has

been suggested in previous works (e.g., Toft et al. 2014; Belli et al. 2019; Forrest et al. 2020).

It now appears that significant numbers of these dust-obscured galaxies exist at $z > 3$, many of which may not be photometrically detected in the optical or even the H and K bandpasses due to large amounts of dust (Wang et al. 2019; Williams et al. 2019; Riechers et al. 2020). The inferred number densities of these objects have also increased as a result of larger and deeper surveys with ALMA (e.g., Riechers et al. 2020) and agree with number densities of UMGs (star-forming and quiescent combined) observed photometrically at $3 < z < 4$, which has been found to be about $N \sim 1 \times 10^{-5} \text{ Mpc}^{-3}$ (Schreiber et al. 2018a; Marsan et al. 2020, in preparation). Of course, because star-forming UMGs contribute to this number density, it is unreasonable to assume that all $z > 5$ DSFGs are quenched by $z = 3$ (see Valentino et al. 2020 for an in-depth discussion), though it seems reasonable to assume that the progenitors of the quiescent UMGs were at one time starbursts very similar to these DSFGs. Best-fit SFHs suggest that this period of intense star formation occurred at $z \gtrsim 4$ for the majority of the UMGs (Figure 10), perhaps also suggesting the existence of fainter, quenched UMGs as descendants of the $z > 5$ DSFG population.

Indeed, the evolution of the most-massive early-type galaxies in the local universe along a path involving rapid star formation as a DSFG at $z > 5$, quenching around $z > 3$, and the subsequent stellar-mass growth via mergers, is supported by several lines of evidence. Studies of local galaxies suggest a scenario in which the most-massive galaxies formed their stars in bursts at very early times (e.g., Kauffmann et al. 2003; Gallazzi et al. 2005; Thomas et al. 2010; Smith et al. 2012), with subsequent mass growth dominated by mergers (Hill et al. 2017). The size growth of quiescent galaxies from compact at high redshift to more extended at lower redshifts is also consistent with being merger driven (e.g., Barro et al. 2013; Kubo et al. 2018; Estrada-Carpenter et al. 2020). The

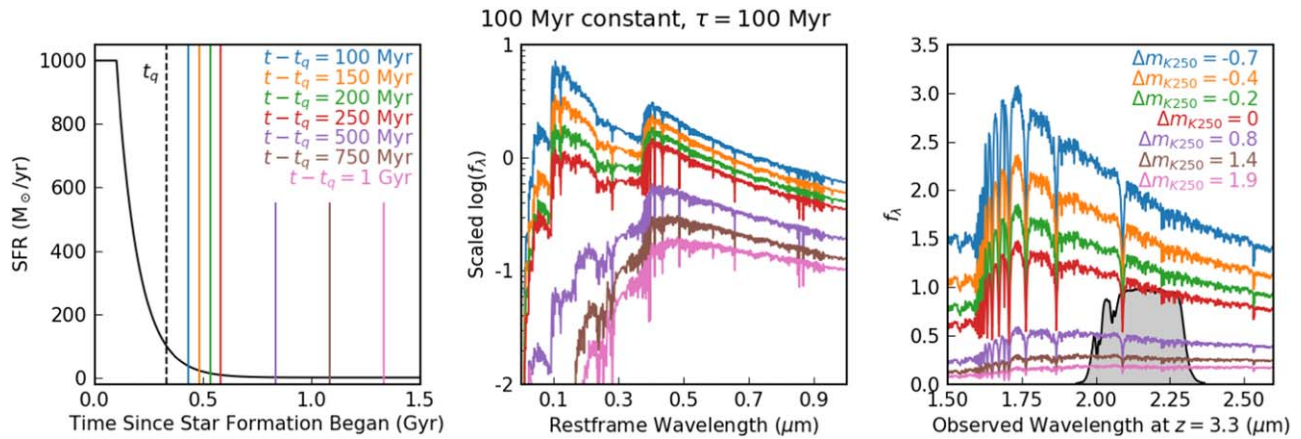


Figure 11. The evolution of K_s -band magnitude for an object with a 100 Myr of constant star formation followed by an exponential decline parameterized by $\tau = 100$ Myr. Left: the SFH (black) used to construct the SEDs at various times (solid, colored lines). The vertical dashed line represents the nominal quenching time, t_q , taken to be when the SFR drops below 10% that of the main starburst period. Center: the resultant SEDs at each time step, corresponding to 100, 150, 200, 250, 500, 750, and 1000 Myr after the quenching time, and scaled relative to the $t - t_q = 250$ Myr SED (red). Right: the SEDs redshifted to $z = 3.3$. The gray curve corresponds to the K_s -band response function, and magnitude differences are given relative to the $t - t_q = 250$ Myr SED (red).

quenching timescales presented here for such a large sample of UMGs at $3 < z < 4$ convincingly support this evolutionary hypothesis of the most-massive galaxies.

5.6.2. On the Possibility of Older, Quiescent Galaxies

The quenching timescales derived for this sample suggest that all the quiescent UMGs are younger post-starburst galaxies and not old, long-dead, passive populations. Indeed, at this epoch, no such old passive populations have been spectroscopically confirmed (D’Eugenio et al. 2020), which we also find when comparing the UMGs presented here to those published in Schreiber et al. (2018a) and Valentino et al. (2020). While the age of the universe at $z > 3$ is quite young, there is still sufficient time for a UMG to have formed its stars, quenched, and evolved passively for perhaps as long as 1 Gyr by $z = 3$, especially given the short timescales on which UMGs at this epoch appear to form their stars (Schreiber et al. 2018a; Forrest et al. 2020; Valentino et al. 2020; Saracco et al. 2020).

Such a galaxy would be considerably fainter than a post-starburst one, however, and selection for spectroscopic follow-up is necessarily biased toward brighter targets. We quantify this magnitude difference by generating galaxy SEDs at various stages of the evolution according to several SFHs using BC03 SPS models. Solar metallicity models are used, as this metallicity has been shown to be roughly appropriate for these massive, early galaxies (Belli et al. 2019; Saracco et al. 2020, submitted). We take the SED at several time steps in this evolution, redshift it to $z = 3.3$ (the median redshift of the sample), and calculate the magnitude in the K_s band (see Figure 11 as well as Appendix E for details). Compared to a baseline observation of 0.25 Gyr after the simulated galaxy quenches (roughly consistent with the quenched UMGs), a galaxy observed 1 Gyr after quenching would be one to two magnitudes fainter in the K_s band depending upon the SFH, corresponding to $m_K \sim 22 - 23$ and fainter than the magnitude cut used here. For an object observed at $z = 3.3$, this would correspond to $z_q = 6.1$ and would require extreme star formation just prior to this time, consistent with the $z = 6.34$ DSFG HFLS-3 (Riechers et al. 2013; Cooray et al. 2014).

Galaxies with the requisite K_s -band magnitudes, photometric redshifts, stellar masses, as well as red UVJ colors do exist in

the UltraVISTA DR3 catalog. There are 56 objects with photometric fits suggesting $3 < z < 4$, $\log(M_*/M_\odot) > 11$, and $\text{SFR} < 10 M_\odot \text{ yr}^{-1}$, 47 of which are fainter than $m_K = 22$. Of the nine brighter targets, we targeted and confirmed three—COS-DR3-84674, COS-DR3-111740, and COS-DR3-201999, two of which are post-starbursts and one of which is at a lower redshift. The faintest of the spectroscopically confirmed UMGs (COS-DR3-179370) has $m_K = 22.14$, but we note that this was confirmed via detection of strong emission lines.

The fainter candidate objects generally have lower photometric S/N, leading to less well-constrained photometric redshifts and template fits. As a result, selecting reliable candidates at fainter magnitudes from the existing photometry for spectroscopic follow-up is more difficult. Targeting these candidate old red galaxies with instruments such as Keck/MOSFIRE would require multiple nights to confirm their redshifts and natures through high S/N detection of stellar continuum features. Still, the intriguing possibility of older, more passive galaxies at this early time does exist. Proving it will require significant time investment either from the ground (several nights on 8–10 m class telescopes) or from space (e.g., *JWST*). Upcoming 30 m class telescopes could also play an important role in confirming these objects as well.

6. Conclusions

We have presented the largest sample to date of spectroscopically confirmed UMGs with $\log(M_*/M_\odot) > 11$ at $z > 3$. The sample is selected from the COSMOS-UltraVISTA and XMM-VIDEO fields, which have a critical combination of impressive depth and area, allowing these catalogs to excel at finding such rare objects. Galaxies with well-defined SEDs were observed as part of the MAGAZ3NE survey with the Keck/MOSFIRE instrument in the K band, where strong emission lines from $H\beta$ and $[O\text{III}]$ are observed in 9/16 UMGs. The H band was also used to confirm redshifts via detection of Balmer series absorption, which is clearly visible in all six UMGs targeted, and also to confirm any $[O\text{II}]$ emission. The confirmation of this population is further evidence that such massive galaxies form the vast majority of their stars early in the universe.

While these UMGs show a wide range of SFRs, at least 5/16 have ceased star formation in the last several hundred Myr (post-starbursts) and 3 others only have residual amounts of new star formation ongoing ($\lesssim 5 M_{\odot} \text{ yr}^{-1}$), which puts them >1 dex below the SFMS for galaxies of this redshift and mass. The remainder are forming at least $10 M_{\odot} \text{ yr}^{-1}$, and two UMGs are consistent with $\text{SFR} \gtrsim 100 M_{\odot} \text{ yr}^{-1}$.

Of those with emission features, seven show line ratios of $[\text{O III}]\lambda 5007/\text{H}\beta > 6$, typically observed in such massive galaxies only with AGN activity. This is consistent with previous studies suggesting that massive galaxies at these early times are often AGN hosts and that AGN feedback may play a significant role in quenching star formation in this population.

We compare the $D_n(4000)$ and $EW_0(\text{H}\delta)$ values for five of the UMGs to high-mass galaxies at lower redshifts as well as stellar evolution models. The most massive galaxies at higher redshifts are younger, with the sample suggesting the bulk of stars were formed <1 Gyr before observation.

The build-up of stellar mass from the best-fit SFHs for some of these UMGs are consistent with $z > 5$ DSFGs, again suggesting that a period of intense star formation is a critical step in the evolution of this population before quenching star formation at $z > 3$. This is also consistent with the SFHs derived for massive local galaxies from stellar archeology.

Fitting the full multiwavelength SEDs (corrected for emission-line contamination) and the near-IR spectroscopy yield best-fit SFHs that similarly indicate that most star formation occurred at $4 < z < 5$ in short-lived, explosive bursts of $500\text{--}3000 M_{\odot} \text{ yr}^{-1}$ for $100\text{--}400$ Myr before quenching rapidly. While several of the UMGs have quenched before $z = 4$ as in Forrest et al. (2020), most UMGs that have quenched their star formation did so around $250\text{--}400$ Myr before observation, and we do not confirm any significantly evolved passive galaxies, implying that post-starbursts are the most evolved galaxies in the massive population at this epoch. However, the possibility of older, more passive galaxies does exist, even at this remarkably early time. Identifying compelling candidates will require deeper NIR photometry, and spectroscopically confirming them will require substantial observations with either large ground-based instruments or sensitive space-based telescopes.

The authors wish to recognize and acknowledge the very significant cultural role and reverence that the summit of

Maunakea has always had within the indigenous Hawaiian community. We are most fortunate to have the opportunity to conduct observations from this mountain. Additionally, we thank the anonymous referee for suggestions that improved the manuscript.

This work is supported by the National Science Foundation through grants AST-1517863, AST-1518257, and AST-1815475; by HST program number GO-15294; and by grant numbers 80NSSC17K0019 and NNX16AN49G issued through the NASA Astrophysics Data Analysis Program (ADAP). Support for program number GO-15294 was provided by NASA through a grant from the Space Telescope Science Institute, which is operated by the Association of Universities for Research in Astronomy, Incorporated, under NASA contract NAS5-26555. Further support was provided by the Faculty Research Fund (FRF) of Tufts University and by Universidad Andrés Bello grant number DI-12-19/R. M.N. acknowledges INAF 1.05.01.86.20 and PRIN MIUR F.OB. 1.05.01.83.08. Data presented herein were obtained using the UCI Remote Observing Facility, made possible by a generous gift from John and Ruth Ann Evans.

This work has relied heavily upon code developed by other people, for which we are quite thankful.

Software: Astropy (Robitaille et al. 2013; Price-Whelan et al. 2018), EAzY (Brammer et al. 2008), FAST (Kriek et al. 2009), FAST++ (Schreiber et al. 2018b), IPython (Pérez & Granger 2007), Matplotlib (Hunter 2007), NumPy (Oliphant & Millma 2006), slinefit (Schreiber et al. 2018a).

Appendix A Summary of Observations

Spectra were taken on Keck/MOSFIRE under the program ‘‘Ultramassive Galaxies and Their Environments at $3 < z < 4$ ’’ (PI: Wilson), which was awarded a total of 11.5 nights over 4 semesters (2018B-2020A). Of these, two nights were lost in their entirety due to weather and a total of about one additional night was lost due to various technical issues and shorter periods of inclement weather. Data from a previous program ‘‘Formation of Massive Quiescent Galaxies’’ (PI: Wilson), which consisted of two half-nights in 2017B, were also used in this analysis. We present the observations by individual mask in Table A1 and by UMG in Table A2.

Table A1
Summary of UMG Candidate Masks Observed by Date

| Field | Observing Night | Mask Name | Filter | Total Integration Time (ks) ^a | Average Seeing (") ^b | Galaxies Targeted |
|-------------------|-----------------|----------------------|--------|--|---------------------------------|-------------------|
| COSMOS-UltraVISTA | 2017 Nov 21 | COS2017 ₃ | K | 8.8 | 0.6 / 0.78 | 15 |
| | 2017 Nov 22 | COS2017 ₅ | K | 7.8 | 0.8 / 0.74 | 13 |
| | 2018 Nov 27 | COS-201999-K1 | K | 7.2 | 1.1 / 0.63 | 21 |
| | 2018 Dec 14 | COS-201999-H1 | H | 5.8 | 1.2 / 1.49 | 12 |
| | | COS-201999-H2 | H | 4.8 | 1.2 / 1.40 | 10 |
| | 2018 Dec 15 | COS-84674-H1 | H | 5.3 | 1.2 / 0.95 | 15 |
| | | COS-84674-H2 | H | 5.3 | 1.2 / 0.94 | 13 |
| | 2019 Feb 28 | COS-195616-K1 | K | 7.9 | 1.3 / 0.89 | 18 |
| | | COS-226441-K1 | K | 5.0 | 1.0 / 0.99 | 22 |
| | 2019 Mar 17 | COS-160748-K1 | K | 3.6 | 0.5 / 0.66 | 18 |
| | | COS-201999-H3 | H | 4.8 | 0.7 / 0.67 | 20 |
| | 2019 Nov 14 | COS-201999-H4 | H | 5.8 | 0.6 / 0.61 | 18 |
| | | COS-84674-H3 | H | 6.2 | 0.5 / 0.65 | 16 |
| | 2019 Dec 08 | COS-79837-K1 | K | 2.9 | 0.5 / 0.74 | 9 |

Table A1
(Continued)

| Field | Observing Night | Mask Name | Filter | Total Integration Time (ks) ^a | Average Seeing (") ^b | Galaxies Targeted |
|-----------|-----------------|----------------------|--------|--|---------------------------------|-------------------|
| | | COS-113684-K1 | K | 3.6 | 0.6 / 0.56 | 6 |
| | | COS-258857-K1 | K | 3.6 | 0.6 / 0.80 | 8 |
| | 2020 Feb 02 | COS-131925-K1w | K | 4.3 | 1.4 / 0.77 | 25 |
| | | COS-111740-K1w | K | 9.4 | 1.4 / 1.40 | 21 |
| | 2020 Feb 03 | COS-258857-K12 | K | 3.6 | 1.0 / 0.65 | 8 |
| | | COS-79837-H1 | K | 12.5 | 0.8 / 0.87 | 9 |
| | | COS-208070-K1 | K | 3.6 | 0.8 / 0.99 | 14 |
| | 2020 Feb 23 | COS-111740-H1 | H | 4.3 | 1.0 / 0.66 | 21 |
| | | COS-208070-K2 | K | 4.3 | 1.0 / 0.80 | 16 |
| | | COS-113684-K2 | K | 8.6 | 0.7 / 0.68 | 6 |
| XMM-VIDEO | 2017 Nov 21 | XMM2017 ₂ | K | 18.5 | 0.8 / 0.89 | 14 |
| | 2017 Nov 22 | XMM2017 ₄ | K | 18.5 | 0.8 / 0.88 | 15 |
| | 2018 Nov 27 | XMM-2599-K1 | K | 10.8 | 0.6 / 0.69 | 21 |
| | 2018 Dec 14 | XMM-2599-H1 | H | 8.6 | 0.6 / 0.94 | 14 |
| | | XMM-2599-H2f | H | 4.8 | 1.0 / 1.46 | 13 |
| | 2018 Dec 15 | XMM-2599-H1f | H | 9.6 | 0.7 / 1.13 | 15 |
| | | XMM-2962-K1 | K | 5.0 | 0.6 / 0.70 | 20 |
| | 2019 Nov 14 | XMM-3941-H1 | H | 5.3 | 0.5 / 1.21 | 17 |
| | 2019 Dec 08 | XMM-3941-K1 | K | 5.8 | 0.8 / 1.20 | 17 |
| | | XMM-2293-K1 | K | 2.9 | 0.8 / 0.88 | 24 |
| | 2020 Feb 03 | XMM-3941-K12 | K | 5.0 | 1.0 / 1.25 | 17 |
| | 2020 Feb 23 | XMM-270-K1w | K | 0.7 | 1.0 / 1.18 | 10 |

Notes.^a All individual K -band exposures were 180 s, while H -band exposures were 120 s.^b The first seeing value is the estimated seeing from MIRA focusing, while the second is an average of the seeing derived from Gaussian fits to 1D spectra of slit stars on the given mask.**Table A2**
Summary of Observations by UMG Candidates Ordered by m_K within a Field

| UMG | Masks (n_K, n_H) | Magnitude | | Int. Time (ks) | | Avg. Seeing (") | | Avg. S/N per Pixel | |
|----------------|----------------------------|-----------|-------|----------------|------|-----------------|---------|--------------------|------|
| | | K | H | K | H | K | H | K | H |
| COS-DR3-160748 | COS-160748* (1,0) | 20.25 | 21.09 | 3.6 | ... | 0.7 | ... | 3.44 | ... |
| COS-DR3-202019 | COS-201999* (1,4) | 20.79 | 21.36 | 5.0 | 21.1 | 0.7 | 0.6-1.5 | 2.04 | 1.92 |
| COS-DR3-131925 | COS-131925* (1,0) | 20.96 | 21.30 | 4.3 | ... | 0.8 | ... | 0.25 | ... |
| COS-DR3-201999 | COS-201999* (1,4) | 21.00 | 21.51 | 7.2 | 21.1 | 0.6 | 0.6-1.5 | 3.01 | 3.73 |
| COS-DR1-79837 | COS-79837* (1,1) | 21.10 | 22.25 | 2.9 | 12.5 | 0.7 | 0.9 | 2.42 | 4.12 |
| COS-DR3-113684 | COS-113684* (2,0) | 21.10 | 22.57 | 12.2 | ... | 0.6-0.7 | ... | 2.64 | ... |
| COS-DR3-111740 | COS-111740* (1,1) | 21.10 | 21.09 | 9.4 | 4.3 | 1.4 | 0.7 | 4.96 | 3.03 |
| COS-DR3-84674 | COS-84674* (0,3) | 21.28 | 21.67 | ... | 16.8 | ... | 1.2 | ... | 4.36 |
| COS-DR3-195616 | COS-195616* (1,0) | 21.64 | 22.34 | 8.1 | ... | 1.3 | ... | 1.63 | ... |
| COS-DR3-226441 | COS-226441* (1,0) | 21.65 | 22.46 | 5.0 | ... | 1.0 | ... | 0.96 | ... |
| COS-DR1-258857 | COS-258857* (2,0) | 21.66 | 22.46 | 7.2 | ... | 0.76-0.8 | ... | 1.30 | ... |
| COS-DR3-208070 | COS-208070* (2,0) | 21.70 | 22.54 | 7.9 | ... | 0.8-1.0 | ... | 2.18 | ... |
| COS-DR3-179370 | COS2017* (2,0) | 22.14 | 23.51 | 16.6 | ... | 0.7-0.8 | ... | 1.19 | ... |
| XMM-VID3-2075 | XMM-2692* (1,0) | 20.79 | 21.94 | 5.0 | ... | 0.7 | ... | 3.51 | ... |
| XMM-VID1-1120 | XMM-2599* (1,3) | 20.97 | 22.44 | 10.8 | 23.0 | 0.7 | 1.0-1.4 | 4.00 | 1.35 |
| XMM-VID1-2399 | XMM2017 ₄ (1,0) | 21.10 | 21.09 | 18.4 | ... | 0.9 | ... | 1.21 | ... |
| XMM-VID3-3941 | XMM-3941* (2,1) | 21.33 | 22.47 | 10.8 | 5.3 | 1.02 | 0.5 | 2.23 | 1.59 |
| XMM-VID3-2293 | XMM-2293* (1,0) | 21.35 | 22.47 | 2.9 | ... | 0.9 | ... | 1.00 | ... |
| XMM-VID2-270 | XMM-270* (1,0) | 21.47 | 22.51 | 0.7 | ... | 1.0 | ... | 0.32 | ... |
| XMM-VID3-2457 | XMM-2599* (1,3) | 21.52 | 22.61 | 10.8 | 23.0 | 0.7 | 1.0-1.4 | 3.40 | 1.30 |
| XMM-VID1-2761 | XMM2017 ₂ (1,0) | 21.74 | 23.22 | 18.5 | ... | 0.9 | ... | 1.68 | ... |

Note. Masks of the same object begin with a UMG indicator, then with a number and band indicator (here represented by an asterisk) appended. The number of masks observed in each bandpass is also given.

Appendix B Observations of Unconfirmed Objects

In this work, we have presented spectra of 16 UMGs. However, five other UMG candidates were also spectroscopically observed, and these objects are presented here. The associated masks and observations for each UMG are included in Table A1 and Table A2. SEDs and spectra are presented in Figure B1.

XMM-VID3-3941 has a very red SED, suggesting significant dust obscuration, and its photometry is well fit with a massive, dusty template at $z_{\text{phot}} = 3.04$. However, it is spectroscopically confirmed to be a quasar at $z_{\text{spec}} = 3.68$. Comparison of the K -band spectrum with the SDSS composite quasar spectrum shows good agreement with broad $H\beta$ and $H\gamma$ emission, as well as narrow $[\text{OIII}]\lambda\lambda 4959, 5007$ emission (Figure B1). Given that the quasar potentially contributes a substantial amount to the flux of this galaxy, we refrain from estimating other properties such as stellar mass.

A photometric redshift analysis indicates that COS-DR1-79837 is also a massive, dusty, star-forming galaxy at $z = 3.3$. Spectra do not reveal clear features to confirm a redshift, though a combined fit to spectra and photometry yields a best-fit $z = 2.65$. The upturn in flux in the IRAC 3.6 μm and 4.5 μm channels is also suggestive of AGN activity.

Both of these candidates lie in the upper-right corner of the UVJ diagram, nominally the location of dusty star-forming galaxies, and have large photometric stellar-mass estimates of $\log(M_*/M_\odot) > 11.7$. Galaxies in this region are difficult to spectroscopically confirm as many observable line features are expected to be obscured by dust. Further probing of this region is warranted and will be explored in future work.

COS-DR1-258857 lies on the wedge separating the star-forming and quiescent regions of the UVJ diagram, with $z_{\text{phot}} = 3.26$. The spectrum shows two significant dips around 2.14 and 2.17 μm , though the spectrum is noisy. Assuming one of these is $H\beta$ absorption, the redshift is then either $z = 3.40$ or $z = 3.46$.

The spectrum of XMM1-2761 does not have sufficient S/N to determine a redshift, though we note this target is very faint ($z_{\text{phot}} = 3.59, m_K = 21.74$). Photometric detections in the rest-frame UV suggest some ongoing star formation. The UVJ colors may incorrectly place this galaxy in the quiescent wedge due to photometric contamination by strong emission lines.

XMM-VID2-270 is photometrically a post-starburst similar to a number of others confirmed in this work. Integration time on this object was exceedingly short, taken in a short period after high winds had subsided and before the XMM field set, and no features are apparent in the resulting spectrum.

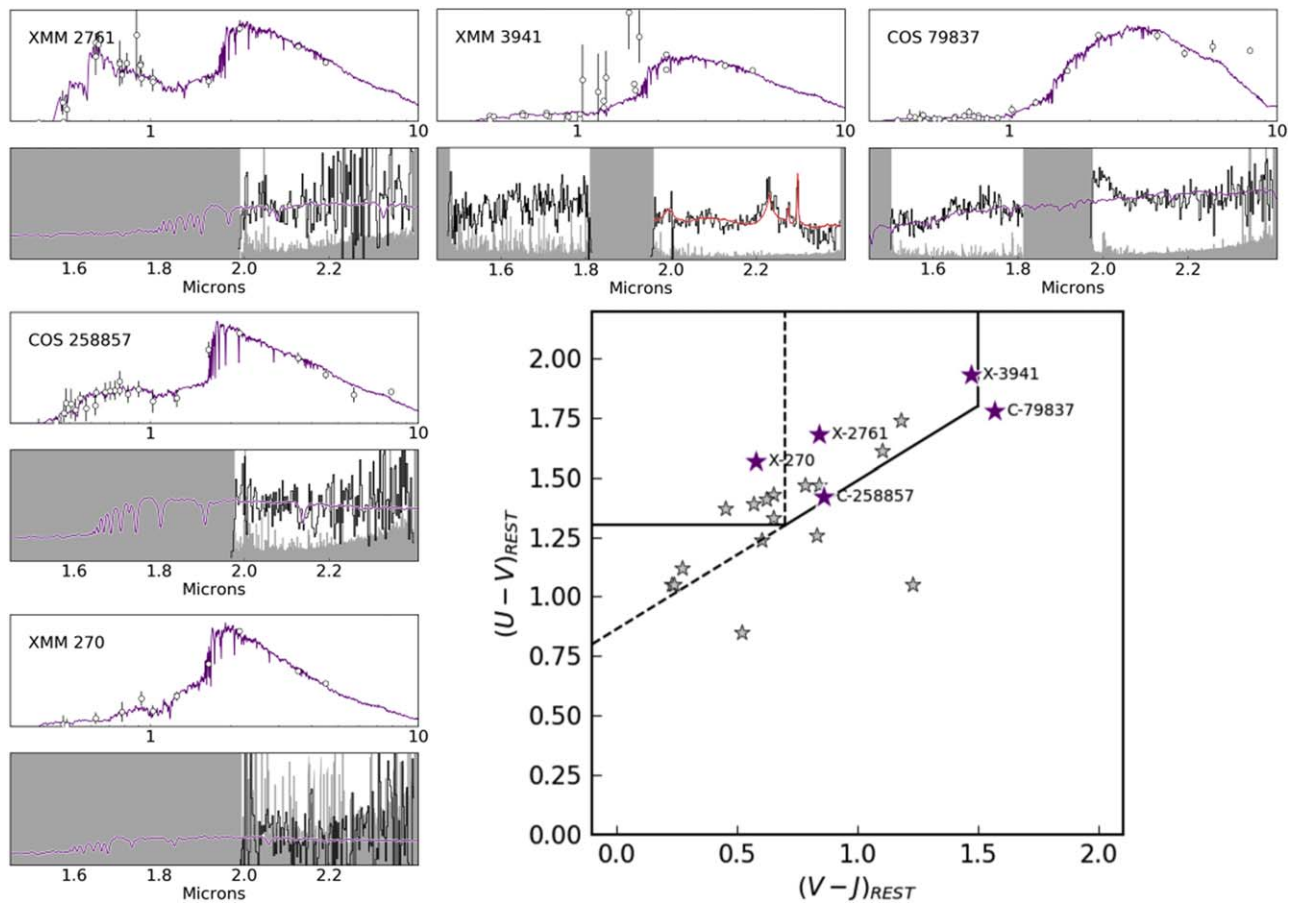


Figure B1. Central panel: the rest-frame UVJ diagram showing the location of the five unconfirmed objects (purple) relative to the 16 confirmed UMGs (gray). Surrounding panels: the photometry (top) and spectroscopy (bottom) for each object, shown with the best-fit template in purple. For XMM-VID3-3941, the SDSS composite quasar template (Vanden Berk et al. 2001) redshifted to $z = 3.59$ is shown in red.

Appendix C Identification of Sky-line Contamination

We use the uncertainties on pixel fluxes determined by the DRP, which we refer to below as pixel variance, to identify sky lines. This is done by comparing the average pixel variance at a given wavelength to the distribution of pixel variances across the entire mask. For each wavelength λ_i in a reduced *H*-band mask, we calculate the median variance per pixel on sky in the spatial direction, $\text{median}(\sigma^2(\lambda_i))$. This is then compared to the distribution of variances across all sky pixels, $\sigma^2(\lambda, s)$. If $\text{median}(\sigma^2(\lambda_i)) > 1.5 \times P_{25}(\sigma^2(\lambda, s))$, where P_n corresponds to the n th percentile, then λ_i is considered to have sky-line contamination. Additionally, if $\text{median}(\sigma^2(\lambda_i)) > 2.5 \times P_{25}(\sigma^2(\lambda, s))$, then λ_i is considered to have contamination from a strong sky line, while between the two thresholds is termed contamination from a weak sky line. Regions with strong lines are masked when doing all fits. We interpolate fluxes over regions with weak lines, but do

not change the variance, which is generally higher at these wavelengths. An example from a portion of an *H*-band mask is shown in Figure C1.

The above method will not work effectively in the *K* band due to increasing thermal contamination at redder wavelengths. Applying the same method would result in incorrectly identifying a large percentage of pixels at $\lambda > 2.2 \mu\text{m}$ as sky lines and failing to identify weak sky lines at bluer wavelengths. In this case, we model the background contribution to variance (i.e., not due to sky lines) at λ_i by calculating a running $P_{10}(\sigma^2(\lambda_i \pm 0.1 \mu\text{m}))$ and taking the ratio with spectral uncertainty. We then perform the same calculation as for the *H*-band masks with this “normalized” variance distribution to determine thresholds for sky-line identification (see Figure C2). In the case of both the *H* band and *K* band (Figure C3), these identifications are checked against visual identification and confirmed to be effective at removing sky-line contamination.

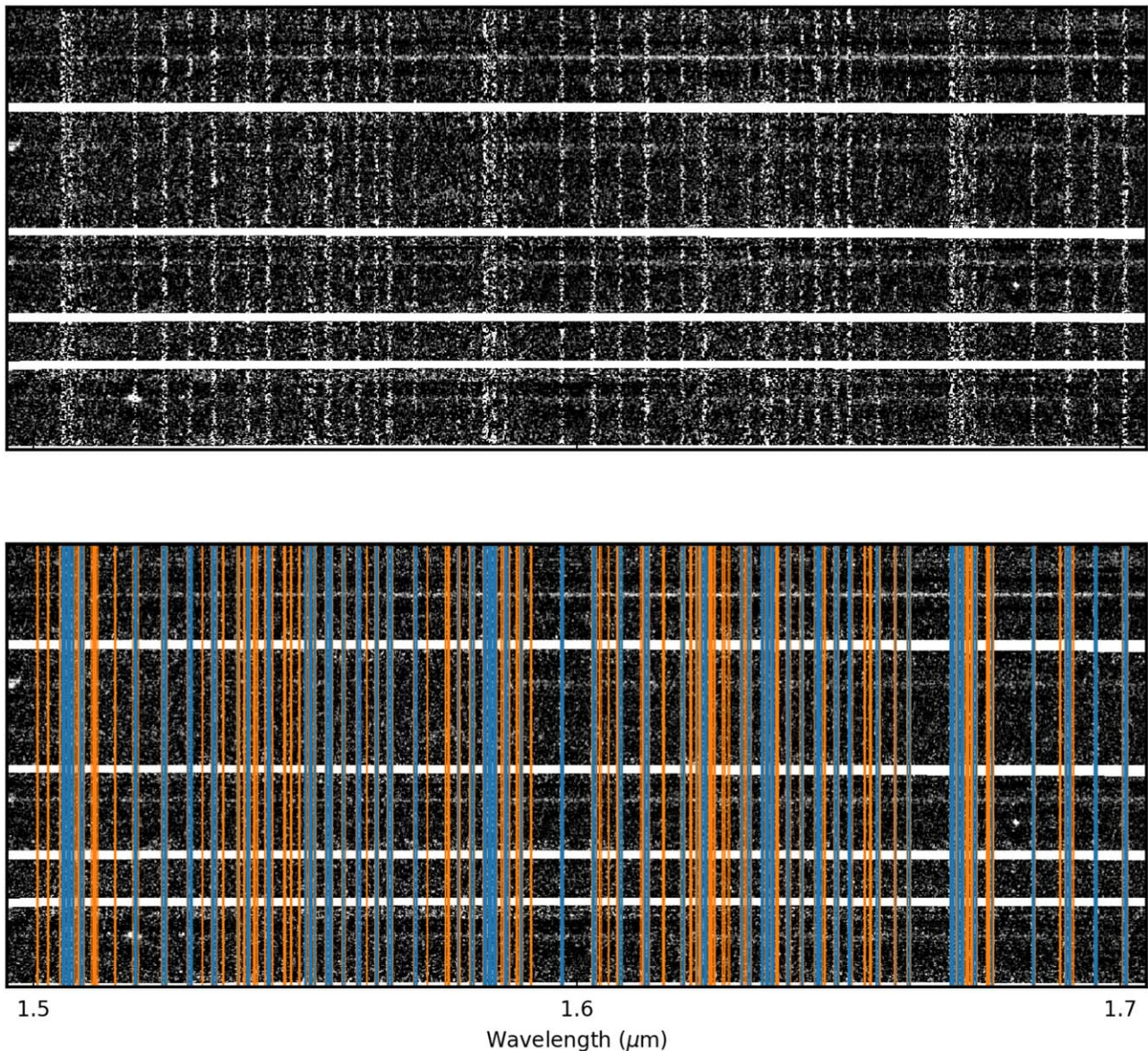


Figure C1. Top: a portion of an example *H*-band mask reduced with the MOSFIRE DRP, with obvious sky lines. Bottom: the results of the sky-line identification—orange are weak sky lines and blue are strong sky lines.

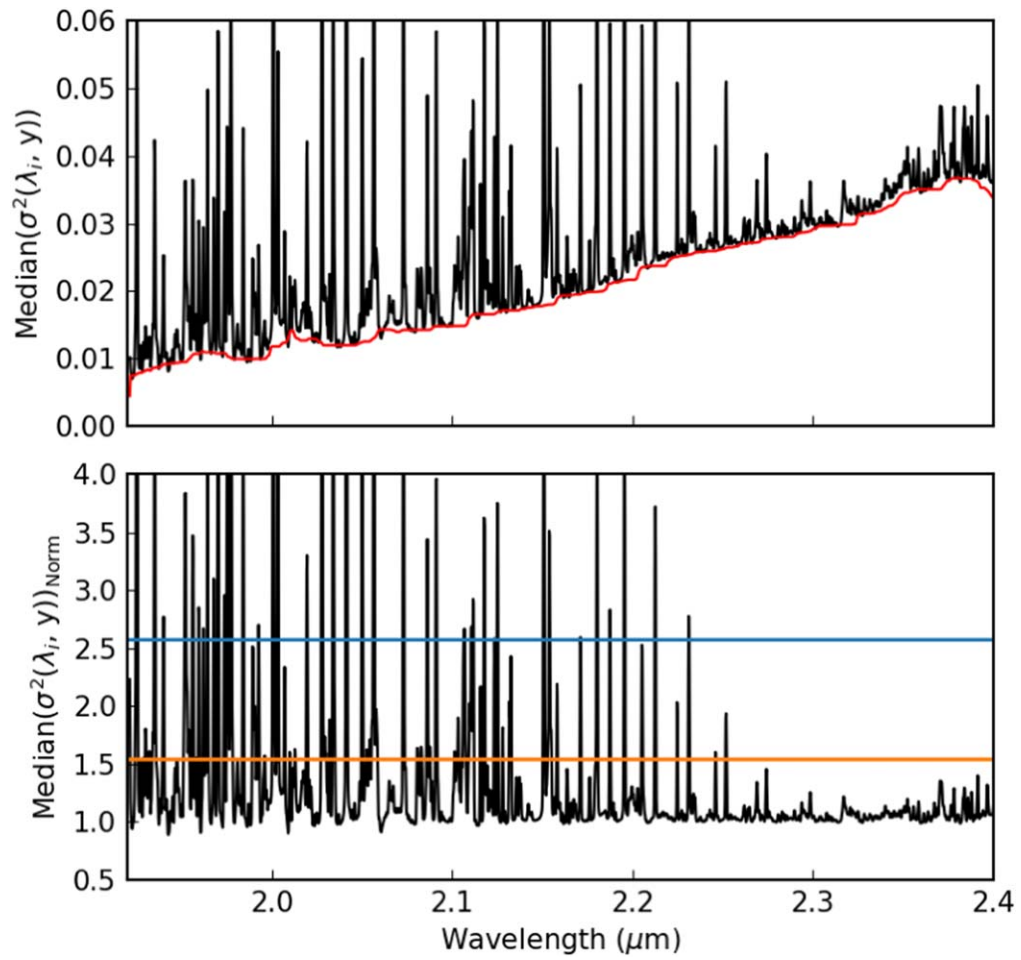


Figure C2. Top: the median variance per pixel across wavelengths for a sample *K*-band mask (black). The value over which we normalize is shown in red. Bottom: the normalized variance per wavelength (black) as well as the thresholds for weak (orange) and strong (blue) sky-line contamination.

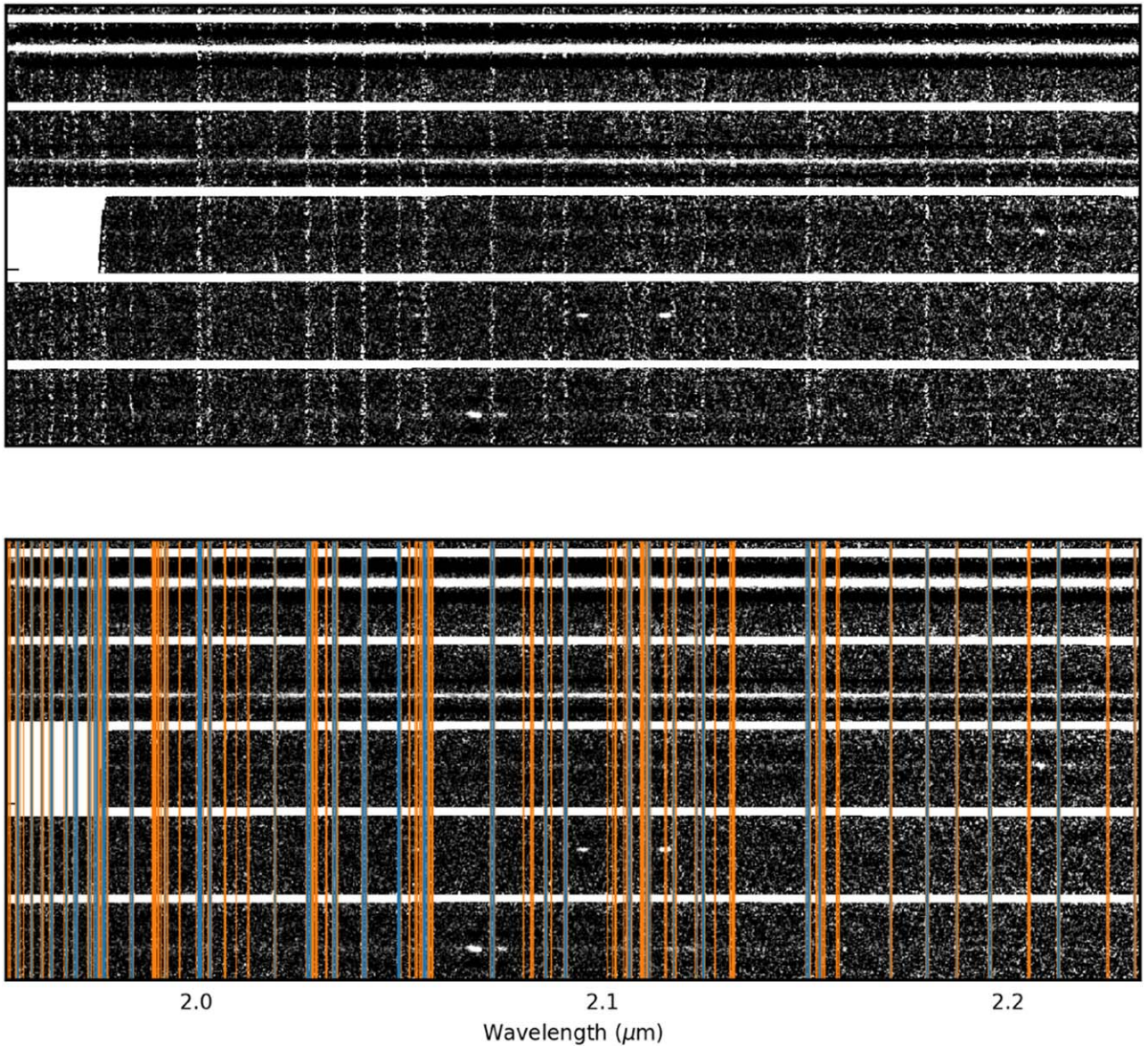


Figure C3. Same as Figure C1 but for a K -band mask, using the normalized variance threshold shown in Figure C2.

Appendix D Telluric Correction Comparison

The telluric correction used in this work involved modeling the observed spectra of faint stars on the individual MOSFIRE masks. Slit stars have previously been used successfully for absolute flux calibrations (e.g., Kriek et al. 2015) and telluric correction (e.g., Schreiber et al. 2018a, see Appendix B for details).

On many nights, we also took spectra of telluric standard stars, all of which were A-type stars, to provide an alternative telluric correction option. These spectra were processed in the same manner as the science masks (MOSFIRE DRP to obtain 2D spectrum, custom code for 1D extraction). We subsequently masked and interpolated over hydrogen absorption features present in the 1D spectra of these stars and compared the resultant curve to a blackbody with the temperature of the same spectral subtype. The normalized ratio of these two yielded a telluric correction factor that was applied to all the spectra on a given mask.

When compared to the method incorporating the slit stars, this method gave generally similar results. The standard star correction tends to be smoother, which is reasonable considering that one part of the ratio (the blackbody) is itself a smooth curve and given the higher S/N of the bright standard star relative to the slit star. For masks observed directly before or after a standard star observation, the differences in the telluric-corrected spectra between the two methods are small (Figure D1). However, we find that the corrections tend to be more discrepant as the time between observations of a mask and a standard star increase, almost certainly due to atmospheric changes throughout the night (Figure D2). To determine the redshifts and locations of strong emission and absorption features, these differences are inconsequential.

We note that for science goals requiring high-S/N spectra, such differences could become relevant. Also we do not claim that one correction is necessarily better than the other, as this will depend on the targets, observing sequence, and observing conditions.

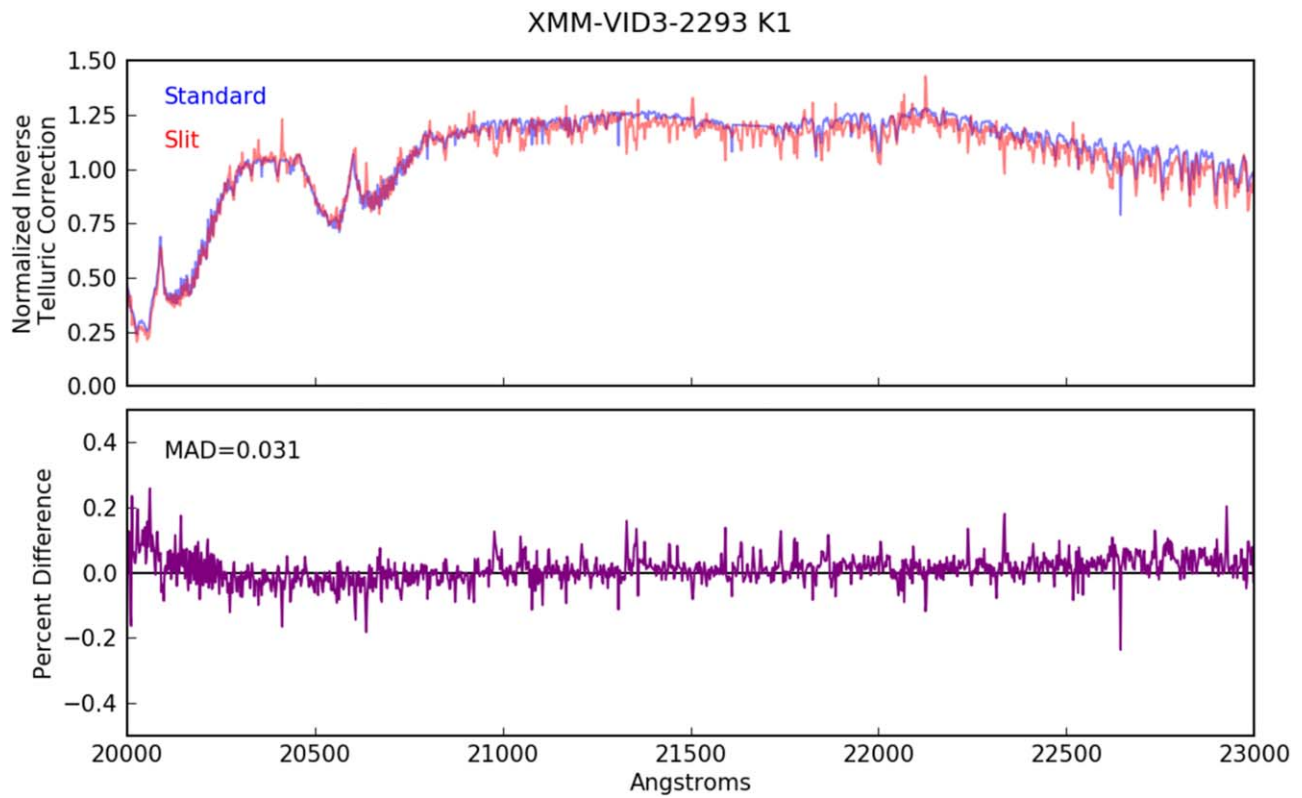


Figure D1. Top: comparison of the telluric correction derived using stars on science slits (red) to the telluric corrections derived using a standard star (blue) observed directly after the mask. Bottom: the percent difference between the two corrections as a function of wavelength. The median absolute deviation is given as well.

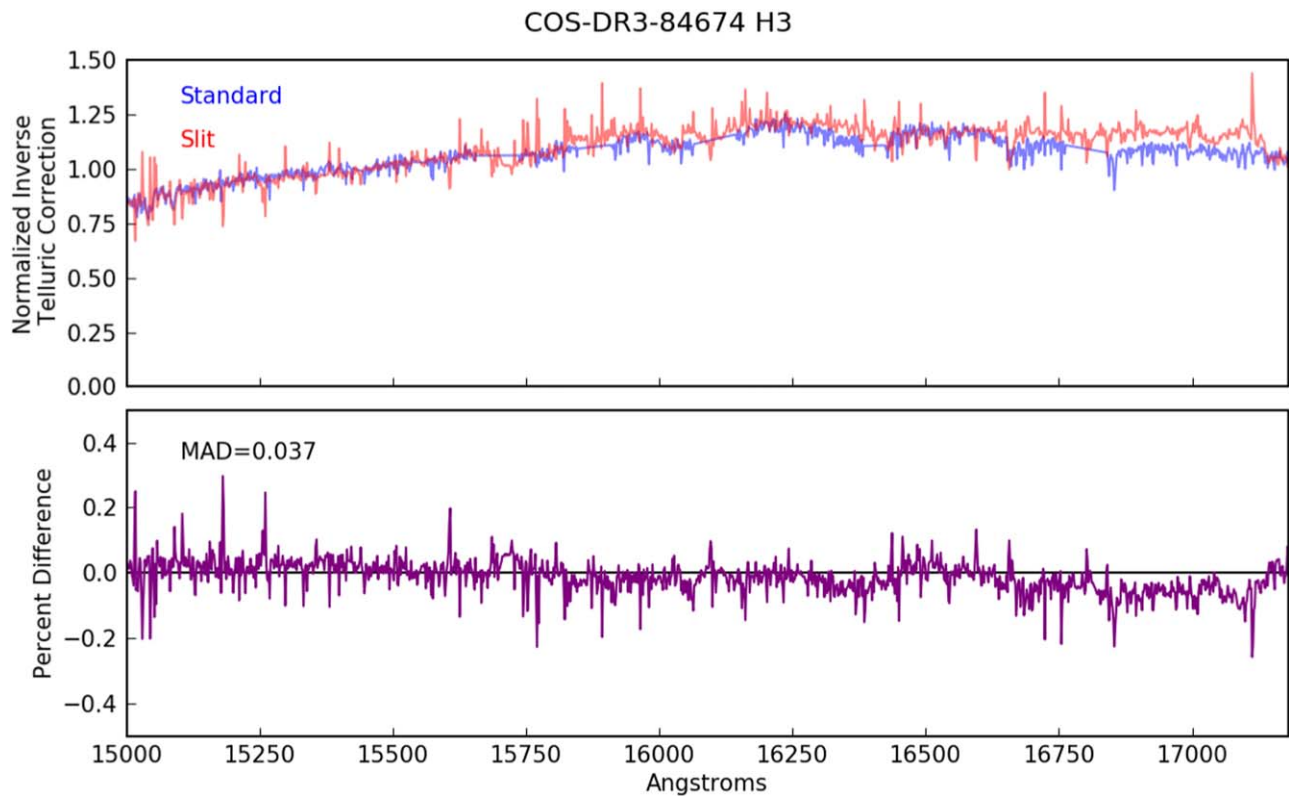


Figure D2. Same as Figure D1, but for a mask that had two hours between observations of the mask and the standard star.

Appendix E

On the Existence of a Population of Older UMGs

As we discuss in Sections 5.5 and 5.6, spectroscopically confirmed massive galaxies at $z > 3$ lacking evidence of star formation appear to be post-starbursts, i.e., have quenched in the last several hundred megayears. Given that detection of these objects is very near the limit of what is possible with current instrumentation, we must consider the fact that this is the result of an observational bias. We explore this by calculating how much fainter an older, passive UMG would be at these redshifts.

To accomplish this, we construct SEDs at various times along several SFHs (using BC03 SPS models) and compare their luminosities in the K_s band, assuming a redshift of $z = 3.3$, the median of the sample. We begin with an SFH consisting of 100 Myr of constant (and vigorous) star formation, followed by a

quick decline in star formation with $\tau = 100$ Myr, shown in Figure 11. The time at which this galaxy quenched is taken to be when star formation drops below 10% of the SFR during the constant period of star formation, akin to the value calculated for the UMGs. This SFH is similar to the best-fit SFHs for the UMGs, which have a median starburst period of 122 Myr and steeply declining SFR thereafter. As expected, we find that galaxies that quenched earlier are significantly redder and fainter, in this case over five times fainter for a galaxy that quenched 1 Gyr before observation.

However, this test is somewhat model dependent. The difference in magnitude due to time since quenching decreases with an increase in either the duration of the starburst period (Figure E1) or the τ parameter (Figure E2). In addition, this limits how long ago the oldest galaxies could have quenched given the young age of the universe (1.9 Gyr at $z = 3.3$).

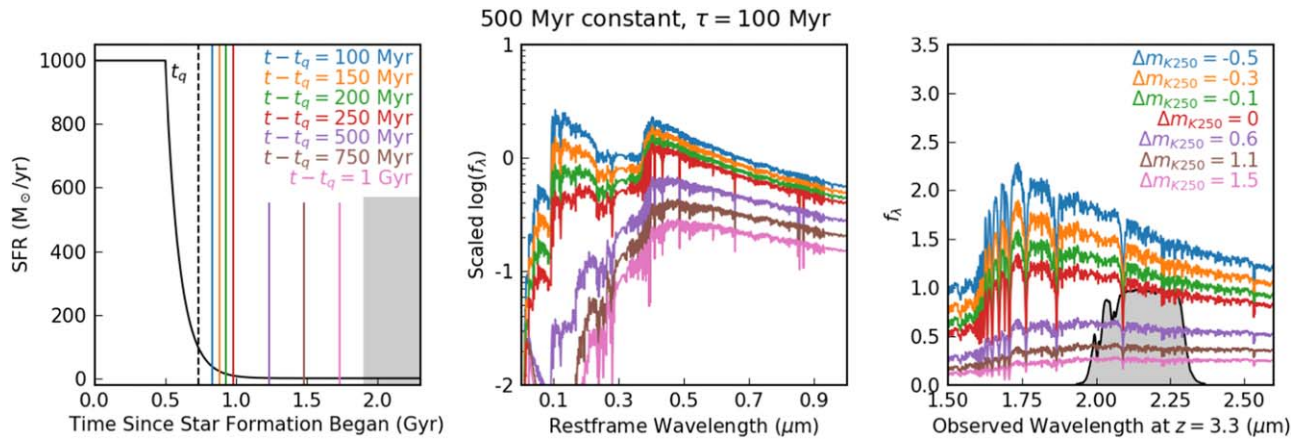


Figure E1. The same as Figure 11 but with an SFH of 500 Myr constant followed by an exponential decline of $\tau = 100$ Myr. The grayed-out region on the left panel indicates an age greater than that of the universe at $z = 3.3$.

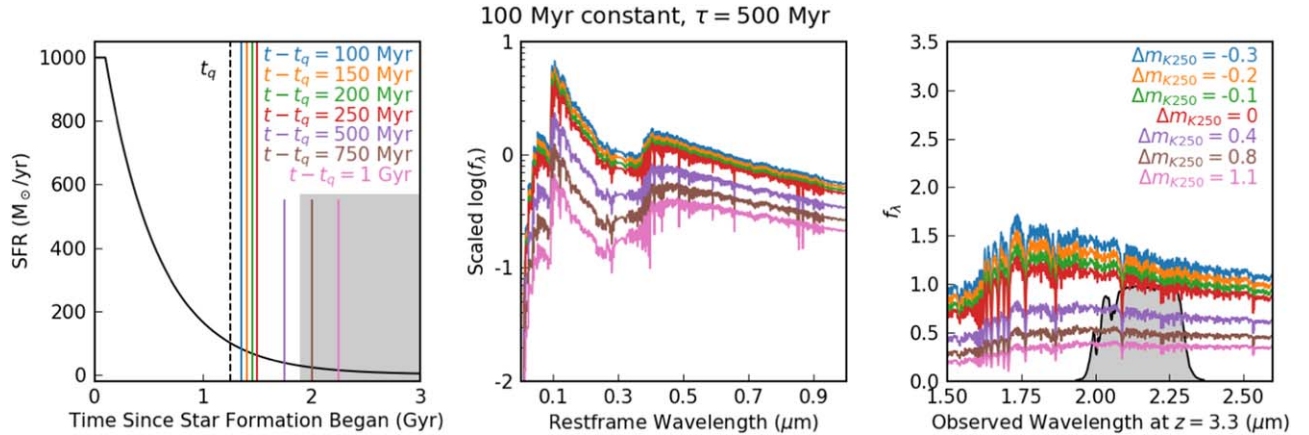
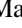

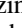

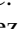

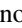
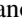
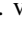


Figure E2. The same as Figure 11 but with an SFH of 100 Myr constant followed by an exponential decline of $\tau = 500$ Myr. The grayed-out region on the left panel indicates an age greater than that of the universe at $z = 3.3$. Assuming star formation began ~ 400 Myr after the Big Bang ($z \sim 11$), this extreme example would have dropped below 10% of its maximum SFR at $z \sim 5$.

ORCID iDs

Ben Forrest  <https://orcid.org/0000-0001-6003-0541>
 Z. Cemile Marsan  <https://orcid.org/0000-0002-7248-1566>
 Gillian Wilson  <https://orcid.org/0000-0002-6572-7089>
 Adam Muzzin  <https://orcid.org/0000-0002-9330-9108>
 Danilo Marchesini  <https://orcid.org/0000-0001-9002-3502>
 M. C. Cooper  <https://orcid.org/0000-0003-1371-6019>
 Jeffrey C. C. Chan  <https://orcid.org/0000-0001-6251-3125>
 Percy Gomez  <https://orcid.org/0000-0003-0408-9850>
 Erin Kado-Fong  <https://orcid.org/0000-0002-0332-177X>
 Francesco La Barbera  <https://orcid.org/0000-0003-1181-6841>
 Julie Nantais  <https://orcid.org/0000-0002-7356-0629>
 Mario Nonino  <https://orcid.org/0000-0001-6342-9662>
 Paolo Saracco  <https://orcid.org/0000-0003-3959-2595>
 Mauro Stefanon  <https://orcid.org/0000-0001-7768-5309>
 Remco F. J. van der Burg  <https://orcid.org/0000-0003-1535-2327>

References

- Alcalde Pampliega, B., Pérez-González, P. G., Barro, G., et al. 2019, *ApJ*, **876**, 135
- Ashby, M. L. N., Caputi, K. I., Cowley, W., et al. 2018, *ApJS*, **237**, 39
- Baldwin, J. A., Phillips, M. M., & Terlevich, R. 1981, *PASP*, **93**, 5
- Balogh, M. L., Morris, S. L., Yee, H. K. C., Carlberg, R. G., & Ellingson, E. 1999, *ApJ*, **527**, 54
- Banerji, M., Jouvel, S., Lin, H., et al. 2015, *MNRAS*, **446**, 2523
- Barro, G., Faber, S. M., Pérez-González, P. G., et al. 2013, *ApJ*, **765**, 104
- Belli, S., Newman, A. B., & Ellis, R. S. 2017, *ApJ*, **834**, 18
- Belli, S., Newman, A. B., & Ellis, R. S. 2019, *ApJ*, **874**, 17
- Belli, S., Newman, A. B., Ellis, R. S., & Konidaris, N. P. 2014, *ApJL*, **788**, L29
- Bellstedt, S., Robotham, A. S. G., Driver, S. P., et al. 2020, *MNRAS*, **498**, 5581
- Brammer, G. B., van Dokkum, P. G., & Coppi, P. 2008, *ApJ*, **686**, 1503
- Bruzual, G., & Charlot, S. 2003, *MNRAS*, **344**, 1000
- Calzetti, D., Armus, L., Bohlin, R. C., et al. 2000, *ApJ*, **533**, 682
- Capak, P. L., Riechers, D., Scoville, N. Z., et al. 2011, *Natur*, **470**, 233
- Chabrier, G. 2003, *PASP*, **115**, 763
- Ciesla, L., Elbaz, D., & Fensch, J. 2017, *A&A*, **608**, A41
- Cimatti, A., Daddi, E., Renzini, A., et al. 2004, *Natur*, **430**, 184
- Cooray, A., Calanog, J., Wardlow, J. L., et al. 2014, *ApJ*, **790**, 40
- Crain, R. A., Schaye, J., Bower, R. G., et al. 2015, *MNRAS*, **450**, 1937
- Davé, R., Thompson, R., & Hopkins, P. F. 2016, *MNRAS*, **462**, 3265
- D'Eugenio, C., Daddi, E., Gobat, R., et al. 2020, *ApJL*, **892**, L2
- Dunlop, J., Peacock, J., Spinrad, H., et al. 1996, *Natur*, **381**, 581
- Einstein, A., & de Sitter, W. 1932, *PNAS*, **18**, 213
- Estrada-Carpenter, V., Papovich, C., Momcheva, I., et al. 2019, *ApJ*, **870**, 133
- Estrada-Carpenter, V., Papovich, C., Momcheva, I., et al. 2020, *ApJ*, **898**, 171
- Feldmann, R., Hopkins, P. F., Quataert, E., Faucher-Giguère, C. A., & Kereš, D. 2016, *MNRAS*, **458**, L14
- Forrest, B., Annunziatella, M., Wilson, G., et al. 2020, *ApJL*, **890**, L1
- Forrest, B., Tran, K.-V. H., Broussard, A., et al. 2018, *ApJ*, **863**, 131
- Forrest, B., Tran, K.-V. H., Tomczak, A. R., et al. 2016, *ApJL*, **818**, L26
- Gallazzi, A., Charlot, S., Brinchmann, J., White, S. D., & Tremonti, C. A. 2005, *MNRAS*, **362**, 41
- Gargiulo, A., Saracco, P., Tamburri, S., Lonoce, I., & Ciocca, F. 2016, *A&A*, **592**, 132
- Genel, S., Vogelsberger, M., Springel, V., et al. 2014, *MNRAS*, **445**, 175
- Glazebrook, K., Schreiber, C., Labbé, I., et al. 2017, *Natur*, **544**, 71
- Gobat, R., Strazzullo, V., Daddi, E., et al. 2012, *ApJL*, **759**, L44
- Grogin, N. A., Kocevski, D. D., Faber, S. M., et al. 2011, *ApJS*, **197**, 35
- Guarnieri, P., Maraston, C., Thomas, D., et al. 2019, *MNRAS*, **483**, 3060
- Henriques, B. M. B., White, S. D. M., Thomas, P. A., et al. 2015, *MNRAS*, **451**, 2663
- Hill, A. R., Muzzin, A., Franx, M., et al. 2017, *ApJ*, **837**, 147
- Hopkins, P. F., Kereš, D., Oñorbe, J., et al. 2014, *MNRAS*, **445**, 581
- Horne, K. 1986, *PASP*, **98**, 609
- Hunter, J. D. 2007, *CSE*, **9**, 90
- Husser, T.-O., Wende-von Berg, S., Dreizler, S., et al. 2013, *A&A*, **553**, A6
- Jafarizayani, M., Newman, A. B., & Mobasher, B. 2020, *ApJL*, **897**, L42
- Jarvis, M. J., Bonfield, D. G., Bruce, V. A., et al. 2013, *MNRAS*, **428**, 1281
- Jin, S., Daddi, E., Magdis, G. E., et al. 2019, *ApJ*, **887**, 144
- Juneau, S., Dickinson, M., Alexander, D. M., & Salim, S. 2011, *ApJ*, **736**, 104
- Kauffmann, G., Heckman, T. M., White, S. D. M., et al. 2003, *MNRAS*, **341**, 54
- Kawinwanichakij, L., Papovich, C., Ciardullo, R., et al. 2020, *ApJ*, **892**, 7
- Kennicutt, R. C. 1998, *ARA&A*, **36**, 189
- Kewley, L. J., Dopita, M. A., Leitherer, C., et al. 2013, *ApJ*, **774**, 100
- Koekemoer, A. M., Faber, S. M., Ferguson, H. C., et al. 2011, *ApJS*, **197**, 36
- Kriek, M., Price, S. H., Conroy, C., et al. 2019, *ApJL*, **880**, L31
- Kriek, M., Shapley, A. E., Reddy, N. A., et al. 2015, *ApJS*, **218**, 1
- Kriek, M., van Dokkum, P. G., Labbé, I., et al. 2009, *ApJ*, **700**, 221
- Kriek, M., van Dokkum, P. G., Whitaker, K. E., et al. 2011, *ApJ*, **743**, 168
- Kubo, M., Tanaka, M., Yabe, K., et al. 2018, *ApJ*, **867**, 1
- Labbé, I., Bouwens, R. J., Illingworth, G. D., & Franx, M. 2006, *ApJL*, **649**, L67
- Labbé, I., Huang, J., Franx, M., et al. 2005, *ApJL*, **624**, L81
- Ma, J., Gonzalez, A. H., Spilker, J. S., et al. 2015, *ApJ*, **812**, 88
- Marchesini, D., Whitaker, K. E., Brammer, G., et al. 2010, *ApJ*, **725**, 1277
- Marrone, D. P., Spilker, J. S., Hayward, C. C., et al. 2018, *Natur*, **553**, 51
- Marsan, Z. C., Marchesini, D., Brammer, G. B., et al. 2015, *ApJ*, **801**, 133
- Marsan, Z. C., Marchesini, D., Brammer, G. B., et al. 2017, *ApJ*, **842**, 21
- Martis, N. S., Marchesini, D., Brammer, G. B., et al. 2016, *ApJL*, **827**, L25
- Mauduit, J.-C., Lacy, M., Farrah, D., et al. 2012, *PASP*, **124**, 1135
- McCracken, H. J., Milvang-Jensen, B., Dunlop, J., et al. 2012, *A&A*, **544**, A156
- McLean, I. S., Steidel, C. C., Epps, H., et al. 2010, *Proc. SPIE*, **7735**, 77351E
- McLean, I. S., Steidel, C. C., Epps, H. W., et al. 2012, *Proc. SPIE*, **8446**, 84460J
- Mehta, V., Scarlata, C., Capak, P., et al. 2018, *ApJS*, **235**, 36
- Merlin, E., Fontana, A., Castellano, M., et al. 2018, *MNRAS*, **473**, 2098
- Merlin, E., Fortuni, F., Torelli, M., et al. 2019, *MNRAS*, **490**, 3309
- Moustakas, J., Kennicutt, R. C., Jr., & Tremonti, C. A. 2006, *ApJ*, **642**, 775
- Muzzin, A., Marchesini, D., Stefanon, M., et al. 2013, *ApJS*, **206**, 8
- Nelan, J. E., Smith, R. J., Hudson, M. J., et al. 2005, *ApJ*, **632**, 137
- Newman, A. B., Belli, S., Ellis, R. S., & Patel, S. G. 2018, *ApJ*, **862**, 125
- Oke, J. B., & Gunn, J. E. 1983, *ApJ*, **266**, 713
- Oliphant, T., & Millma, J. K. 2006, *CSE*, **9**, 10
- Pacifici, C., Kassin, S. A., Weiner, B. J., et al. 2016, *ApJ*, **832**, 79
- Pavesi, R., Riechers, D. A., Sharon, C. E., et al. 2018, *ApJ*, **861**, 43
- Pérez, F., & Granger, B. E. 2007, *CSE*, **9**, 21
- Price-Whelan, A. M., Sipőcz, B. M., Günther, H. M., et al. 2018, *AJ*, **156**, 123
- Reddy, N. A., Shapley, A. E., Sanders, R. L., et al. 2018, *ApJ*, **869**, 92
- Riechers, D. A., Bradford, C. M., Clements, D. L., et al. 2013, *Natur*, **496**, 329
- Riechers, D. A., Hodge, J. A., Pavesi, R., et al. 2020, *ApJ*, **895**, 81
- Riechers, D. A., Leung, T. K. D., Ivison, R. J., et al. 2017, *ApJ*, **850**, 1
- Robitaille, T. P., Tollerud, E. J., Greenfield, P., et al. 2013, *A&A*, **558**, A33
- Salmon, B., Papovich, C., Finkelstein, S. L., et al. 2015, *ApJ*, **799**, 183
- Sanders, D. B., Salvato, M., Aussel, H., et al. 2007, *ApJS*, **172**, 86
- Schaye, J., Crain, R. A., Bower, R. G., et al. 2015, *MNRAS*, **446**, 521
- Schreiber, C., Glazebrook, K., Nanayakkara, T., et al. 2018a, *A&A*, **618**, A85
- Schreiber, C., Labbé, I., Glazebrook, K., et al. 2018b, *A&A*, **611**, A22
- Shahidi, A., Mobasher, B., Nayyeri, H., et al. 2020, *ApJ*, **897**, 44
- Shapley, A. E., Reddy, N. A., Kriek, M., et al. 2015, *ApJ*, **801**, 88
- Silverman, J. D., Lamareille, F., Maier, C., et al. 2009, *ApJ*, **696**, 396
- Smith, R. J., Lucey, J. R., Price, J., Hudson, M. J., & Phillipps, S. 2012, *MNRAS*, **419**, 3167
- Spitler, L. R., Straatman, C. M. S., Labbé, I., et al. 2014, *ApJL*, **787**, L36
- Straatman, C. M. S., Labbé, I., Spitler, L. R., et al. 2014, *ApJL*, **783**, L14
- Straatman, C. M. S., Spitler, L. R., Quadri, R. F., et al. 2016, *ApJ*, **830**, 51
- Strandet, M. L., Weiss, A., Breuck, C. D., et al. 2017, *ApJL*, **842**, L15
- Strom, A. L., Steidel, C. C., Rudie, G. C., et al. 2017, *ApJ*, **836**, 164
- Tanaka, M., Valentino, F., Toft, S., et al. 2019, *ApJL*, **885**, L34
- Thomas, D., Maraston, C., Bender, R., & de Oliveira, C. M. 2005, *ApJ*, **621**, 673
- Thomas, D., Maraston, C., Schawinski, K., Sarzi, M., & Silk, J. 2010, *MNRAS*, **404**, 1775
- Toft, S., Smolčić, V., Magnelli, B., et al. 2014, *ApJ*, **782**, 68
- Treu, T., Ellis, R. S., Liao, T. X., & van Dokkum, P. G. 2005, *ApJL*, **622**, L5
- Trump, J. R., Konidaris, N. P., Barro, G., et al. 2013, *ApJL*, **763**, 1

- Valentino, F., Tanaka, M., Davidzon, I., et al. 2020, [ApJ](#), 889, 93
- van de Sande, J., Kriek, M., Franx, M., et al. 2013, [ApJ](#), 771, 85
- van der Wel, A., Franx, M., van Dokkum, P. G., et al. 2014, [ApJ](#), 788, 28
- van Dokkum, P. G., Labbé, I., Marchesini, D., et al. 2009, [PASP](#), 121, 2
- Vanden Berk, D. E., Richards, G. T., Bauer, A., et al. 2001, [AJ](#), 122, 549
- Vogelsberger, M., Genel, S., Springel, V., et al. 2014a, [Natur](#), 509, 177
- Vogelsberger, M., Genel, S., Springel, V., et al. 2014b, [MNRAS](#), 444, 1518
- Wang, T., Schreiber, C., Elbaz, D., et al. 2019, [Natur](#), 572, 211
- Wellons, S., Torrey, P., Ma, C.-P., et al. 2015, [MNRAS](#), 449, 361
- Whitaker, K. E., Labbé, I., van Dokkum, P. G., et al. 2011, [ApJ](#), 735, 86
- Williams, C. C., Labbe, I., Spilker, J., et al. 2019, [ApJ](#), 884, 154
- Williams, R. J., Quadri, R. F., Franx, M., van Dokkum, P., & Labbé, I. 2009, [ApJ](#), 691, 1879
- Wu, P.-F., van der Wel, A., Gallazzi, A., et al. 2018, [ApJ](#), 855, 85
- Wuyts, S., Labbe, I., Franx, M., et al. 2007, [ApJ](#), 655, 51
- Zavala, J. A., Montaña, A., Hughes, D. H., et al. 2018, [NatAs](#), 2, 56